University of Helsinki Report Series in Physics

HU-P-D140

X-ray and neutron scattering studies on some nanoscale structures in molecular biology

Teemu Ikonen

Division of X-ray Physics
Department of Physical Sciences
Faculty of Science
University of Helsinki
Helsinki, Finland

ACADEMIC DISSERTATION

To be presented, with the permission of the Faculty of Science of the University of Helsinki for public criticism in Auditorium E204 of the Department of Physical Sciences (Physicum) on 2007-05-19 at 12 o'clock noon.

Helsinki 2007

Supervisor

Professor Ritva Serimaa
Department of Physical Sciences
University of Helsinki
Helsinki, Finland

Reviewers

Professor Jouko Korppi-Tommola
Department of Chemistry
University of Jyväskylä
Jyväskylä, Finland

Docent A. C. Papageorgiou
Turku Centre for Biotechnology
Turku, Finland

Opponent

Professor Teodor Silviu Balaban
Forschungszentrum Karlsruhe
Institute for Nanotechnology
Karlsruhe, Germany

Report Series in Physics HU-P-D140
ISBN 978-952-10-3245-5
ISSN 0356-0961
ISBN 978-952-10-3246-2 (pdf-version)
http://ethesis.helsinki.fi
Helsinki 2007
Yliopistopaino

Abstract

T. Ikonen: X-ray and neutron scattering studies on some nanoscale structures in molecular biology, University of Helsinki, 2007, 49 pages + appendices. University of Helsinki, Report Series in Physics, HU-P-D140, ISBN 978-952-10-3245-5, ISSN 0356-0961, ISBN 978-952-10-3246-2 (pdf-version), Yliopistopaino, Helsinki.

Scattering of X-rays and neutrons has been applied to the study of nanostructures with interesting biological functions. The systems studied were the protein calmodulin and its complexes, bacterial virus bacteriophage ϕ6, and the photosynthetic antenna complex from green sulfur bacteria, chlorosome. Information gathered using various other structure determination methods has been combined to the low resolution information obtained from solution scattering.

Conformational changes in calmodulin-ligand complex were studied by combining the directional information obtained from residual dipole couplings in nuclear magnetic resonance to the size information obtained from small-angle X-ray scattering from solution.

The locations of non-structural protein components in a model of bacteriophage ϕ6, based mainly on electron microscopy, were determined by neutron scattering, deuterium labeling and contrast variation.

New data are presented on the structure of the photosynthetic antenna complex of green sulfur bacteria and filamentous anoxygenic phototrophs, also known as the chlorosome. The X-ray scattering and electron cryomicroscopy results from this system are interpreted in the context of a new structural model detailed in the third paper of this dissertation. The model is found to be consistent with the results obtained from various chlorosome containing bacteria. The effect of carotenoid synthesis on the chlorosome structure and self-assembly are studied by carotenoid extraction, biosynthesis inhibition and genetic manipulation of the enzymes involved in carotenoid biosynthesis. Carotenoid composition and content are found to have a marked effect on the structural parameters and morphology of chlorosomes.

Keywords: X-ray scattering, neutron scattering, SAXS, SANS, contrast variation, NMR, residual dipolar coupling, double-stranded RNA, bacteriophage ϕ6, electron cryomicroscopy, green photosynthetic bacteria, green sulfur bacteria, filamentous anoxygenic phototrophs, bacteriochlorophyll, carotenoid, chlorosome

Preface

This work is based on research conducted at the Division of X-ray Physics, Department of Physical Sciences, University of Helsinki, the EM-unit of the Institute of Biotechnology, University of Helsinki and at various neutron and synchrotron radiation beamlines in Europe, especially beamline D22 at Institute Laue-Langevin in Grenoble and beamline A2 at Hasylab, Hamburg. Colleagues working at these institutes are gratefully acknowledged for their collaboration and for allowing me to use the excellent working facilities of these research centers. I especially have to thank Professor Juhani Keinonen, Head of the Department of Physical Sciences, Professor Keijo Hämäläinen, Head of the Division of X-ray Physics and Professor Seppo Manninen, former Head of the Division of X-ray Physics for the opportunity to work in the organizations they lead.

My biggest thanks go to the coauthors of the papers in this dissertation, all 19 of you who are mentioned in the list of articles at page 6. Without you, this work would not exist. Roman Tuma and Jakub Psencik deserve a special mention for being the driving forces in the chlorosome project.

The personnel of the Division of X-ray Physics are thanked for pleasant lunches and coffee breaks, and for the occasional scientific discussion. Professor Ritva Serimaa is thanked for the quality control and supervision of this work and Doc. Mika Torkkeli for always having an answer to my questions, whether they were about small-angle X-ray scattering or bicycling.

This work was funded by the Academy of Finland, mostly through the National Graduate School in Informational and Structural Biology, and by University of Helsinki.

Hamburg, easter 2007

Teemu Ikonen

Table of contents

List of articles and authors contribution

This dissertation consists of an introductory part followed by five papers. Their publication details and the authors contribution are given below. The articles are referred to by roman numerals throughout the introductory part.

I. Maija-Liisa Mattinen, Kimmo Pääkkönen, Teemu Ikonen, Jeremy Craven, Torbjörn Drakenberg, Ritva Serimaa, Jonathan Waltho, Arto Annila: *Quaternary Structure Built from Subunits Combining NMR and Small-Angle X-Ray Scattering Data*, Biophysical Journal 83(2), 1177-1183 (2002)
`http://www.biophysj.org/cgi/content/full/83/2/1177`
The author wrote the computer code used in optimization of the structure against small-angle scattering data and the parts of the paper describing the small-angle scattering measurements and data analysis.

II. Teemu Ikonen, Denis Kainov, Peter Timmins, Ritva Serimaa, Roman Tuma: *Locating the minor components of double-stranded RNA bacteriophage ϕ6 by neutron scattering*, Journal of Applied Crystallography 36(1), 525-529 (2003)
`http://scripts.iucr.org/cgi-bin/paper?S0021889803001857`
The author made the neutron scattering experiments, data reduction, analysis and modeling.

III. Jakub Psencik, Teemu P. Ikonen, Pasi Laurinmäki, Michael C. Merckel, Sarah J. Butcher, Ritva E. Serimaa, Roman Tuma: *Lamellar Organization of Pigments in Chlorosomes, the Light Harvesting Complexes of Green Photosynthetic Bacteria*, Biophysical Journal 87, 1165-1172 (2004)
`http://www.biophysj.org/cgi/content/full/87/2/1165`
The author made the X-ray scattering experiments, part of the electron cryomicroscopy work, analyzed the X-ray data and based on that, developed a model for the fine structure of BChl aggregates.

IV. Jakub Psencik, Juan B. Arellano, Teemu P. Ikonen, Carles M. Borrego, Pasi A. Laurinmäki, Sarah J. Butcher, Ritva E. Serimaa, Roman Tuma: *Internal Structure of Chlorosomes from Brown-Colored Chlorobium Species and the Role of Carotenoids in Their Assembly*, Biophysical Journal 91, 1433-1440 (2006)
`http://www.biophysj.org/cgi/content/full/91/4/1433`
The author made the X-ray scattering measurements and analyzed the X-ray data.

V. Teemu P. Ikonen, Hui Li, Jakub Psencik, Pasi A. Laurinmäki, Sarah J. Butcher, Niels-Ulrik Frigard, Ritva E. Serimaa, Donald E. Bryant, Roman Tuma: *X-ray scattering and electron cryomicroscopy study on the effect of carotenoid biosynthesis to the structure of C. tepidum chlorosomes*, accepted to Biophysical Journal
The author made the X-ray scattering measurements, analyzed the data and wrote most of the paper.

Symbols and abbreviations

Da	Dalton, unit of mass equivalent to atomic mass unit	10
NMR	nuclear magnetic resonance	10
ds	double-stranded	11
RNA	ribonucleic acid	11
ATP	adenosine triphosphate	11
ss	single-stranded	11
NTP	nucleotide triphospate	11
FMO	Fenna-Matthews-Olson complex	13
Csm	chlorosomal protein	13
BChl	bacteriochlorophyll	13
EM	electron microscopy	15
k	wave vector	16
$\frac{\mathrm{d}\sigma}{\mathrm{d}\Omega}$	differential cross-section	16
f	scattering amplitude	16
q	scattering vector	16
ρ	scattering length density	16
r_0	classical eletron radius	17
τ	attenuation length	17
TEM	transmission electron microscopy	20
SAS	small-angle scattering	20
$I, \frac{\mathrm{d}\Sigma}{\mathrm{d}\Omega}$	intensity, or macroscopic cross-section	20
V_s	irradiated volume of the sample	21
$V_s\gamma(\boldsymbol{r})$	characteristic, or Patterson function	21
$p(r)$	distance distribution function, orientationally averaged Patterson	21
V	particle volume	22
N_A	Avogadro's number	22
BSA	bovine serum albumin	22
R_g	radius of gyration	23
Q	Porod invariant	23
S	particle surface area	24
$P(\boldsymbol{q})$	form factor of a particle	25
J_0, J_1	Bessel functions of the first kind	25
D_2O	deuterium oxide, heavy water	27
ESRF	European Synchrotron Radiation Facility	28
DESY	Deutsches Elektronen Synchrotron	30
SAXS	small-angle X-ray scattering	30
CCD	charge-coupled device	31
SANS	small-angle neutron scattering	31
HRTEM	high-resolution transmission electron microscopy	32
PDB	Protein Data Bank	33
HBP	2-hydroxybiphenyl	36
HPLC	high performance liquid chromatography	36
FWHM	full width at half-maximum	40

1 Introduction

This dissertation presents work on structural biology made with methods suitable for non-crystalline material. The five articles in which the results are published can be divided into a study on methodology in which large structures are constructed from subunits (article I), work on structural virology which hopefully has some relevance for the biology of bacteriophages (article II) and studies of photosynthetic antenna complexes (articles III-V).

The methods are mostly based on elastic scattering of radiation with subnanometer wavelengths. X-rays, neutrons and electrons all have the property of interacting with matter in a non-localised way which allows them to bring structural information from macroscopic areas with atomic resolution. The information encoded into the scattered wave can be deciphered by various methods. Physical focusing of the waves to form a magnified image of a microscopic region gives direct real space information, but this method is limited to scattering of electrons or low energy photons, for which lenses preserving the coherence of the wave exist. Of these methods, transmission electron microscopy has been used extensively in the last three articles of this dissertation. Computational direct inversion of the amplitude of scattered X-rays has been shown to work with biological matter (Shapiro et al. 2005), but is presently also limited to long wavelengths and low resolutions, due to strict coherence demands on the radiation source. The traditional method of analysing scattering data relies on the time-tested theories of diffraction from bulk matter and the specific approximations which are valid for non-crystalline samples and large structures. Applying these methods has been the part of the author in the research described in this dissertation.

The major results of this work relate to the structures involved in photosynthesis, specifically, to the photosynthetic antenna complex found in certain anoxygenic bacteria, chlorosome. The chlorosome is both the largest antenna complex found in nature and also the only one for which definitive model of its structure is lacking. This is of course not a coincidence, since the high-resolution methods in structural biology today work best with small and well ordered units, of which chlorosome is neither. The results in this dissertation do not present a definitive solution to the problem of chlorosome structure, but nevertheless bring with them novel points of view. The chlorosome will thus remain a challenge both with regards to its structure and its biology.

It is worthwhile to remember that the majority of energy consumed in the world originates from the energetic chemical bonds created by photosynthetic organisms during geological timescales. Today, reserves of fossil fuels are reduced with an increasing rate which surpasses the rate by which they were created thousands of times over. The equation with limited resources on one side and growing demand on the other has currently no solution. Understanding the natural processes which have captured the energy of sunlight already for millions of years can perhaps help to solve this problem in the future.

2 Materials

2.1 Calmodulin

Various processes inside eukaryotic cells are regulated by a signal transduction pathway involving Ca^{2+} ions. Muscle contraction, neurotransmitter release and mitosis are examples of functions involving calcium regulation, but many more exist. An essential component in calcium signaling is calmodulin, a small 16.7 kDa protein found conserved in nearly all eukaryotes. Calmodulin has two nearly symmetric globular domains connected with a flexible α-helical linker. Both domains have two EF-hand motifs which bind one Ca^{2+} each. Increase in calcium ion concentration inside the cytosol causes calmodulin to bind to the ions and change conformation, exposing hydrophobic regions in the domains (Babu et al. 1988). These structural changes enable the binding of calmodulin to a large number of enzymes, and by doing so activate these enzymes to function in the next level of the signaling cascade.

Binding of calmodulin to a site in the target enzyme is accompanied by another conformational change in which the two domains, separated by a straight helical linker domain in the unbound Ca^{2+} activated state, are brought closer together. This binding is not very specific and the conformational change can also be accomplished with small molecule ligands, such as trifluoroperazine (Vandonselaar et al. 1994).

The binding to trifluoroperazine (also used as an anti-psychotic drug) prevents interaction with the target enzyme and causes the elongated shape of unbound calmodulin to collapse into a globular form. Small size, easily achieved conformational change and the ubiquitousness and importance of calcium signaling have made calmodulin the favourite of many biophysical and bioinformatics studies. Article I of this dissertation describes a method of constructing molecular complexes from known subunit structures with measurements of the complex made in solution. NMR residual dipolar couplings and small-angle X-ray scattering are combined to get complementary information on the relative positions and orientations of the subunits. Calmodulin in its trifluoroperazine-bound conformation is used as an example of the unknown structure which is determined with the method.

2.2 Bacteriophage $\phi 6$

Bacteriophages, i.e. viruses which infect bacteria, have long been one of the favoured model systems in molecular biology. Being non-pathogenic (for humans) and easily cultivated they form an experimentally accessible example of life at

the simplest level. While they are extremely important in fundamental research, also practical applications of phages exist. Despite the large differences in eukaryotic and prokaryotic cells, much can be learned from the molecular mechanisms of phage infection which can be used in treatment of human and veterinary diseases. Understanding the process of viral infection, i.e. the transport of viral genome through the outer defences of the cells, is naturally of great importance in devising cures for viral diseases. An intriguing possibility is the use of virus-derived nanoparticles as vectors in gene therapy. Antibiotic resistance is a growing problem in a world where hospitals are overcrowded and unnecessary prescription of medication is rampant. A clever approach in the treatment of infections caused by resistant bacteria is to use the natural enemies of bacteria, phages, against them. Bacteriophage therapy has a long history, but its development was slowed down after the phenomenal early success of antibiotics (Merril et al. 2003). Emergence of multiple-resistant strains of common bacteria in human flora, such as *Staphylococcus aureus* has, however, given new focus on research in alternative treatments of bacterial infection.

The bacteriophage $\phi 6$ is a lipid membrane coated double stranded (ds) RNA virus belonging to the *Cystoviridiae* family (Vidaver et al. 1973). Its host organisms are bacteria from genus *Pseudomonas*, mainly *P. phaseolicola*. The dsRNA genome of the $\phi 6$ consists of three segments, named S, M and L, in order of increasing size. The 14 open reading frames in the genome correspond to proteins named P1 to P14. Proteins P1, P2, P4, and P7 form the core of the virus, known as the procapsid, which can in the presence of ATP pack single stranded (ss) RNA genome to form a polymerase complex (Mindich 1988, Mindich and Bamford 1988). Replication of the ssRNA genome inside the polymerase complex and coating of the core by protein P8 make the structure into a dsRNA containing nucleocapsid, which is infectious (Olkkonen et al. 1990).

Of the procapsid proteins P1 is known to be the major structural component, forming a shell with 120 copies per procapsid (Olkkonen and Bamford 1987). P2 is an RNA polymerase with 12 copies per unit (Makeyev and Bamford 2000) and P7 with 60 copies has been shown to be involved in the packaging of RNA (Juuti and Bamford 1997). The NTPase P4 is a hexamer located at the five-fold axes of the procapsid and it is the molecular motor which turns chemical energy to the linear movement of RNA during packaging (de Haas et al. 1999). For a high-resolution structure of P4 from a closely related bacteriophage $\phi 12$ see (Mancini et al. 2004).

From the viewpoint of methodology of structural biology, the $\phi 6$ procapsid is interesting because of the existence of a complete *in vitro* assembly system (Poranen et al. 2001). This feat of "creating life in a test tube" was first achieved by (Fraenkel-Conrat and Williams 1955) with the tobacco mosaic virus which in comparison to $\phi 6$ is simple, consisting of only a single type of protein and ssRNA. Reconstruction of a biologically active unit from its constituents allows the selective manipulation of different components. The classic example of this is the ribosome. The reconstitution of a functional ribosome from subunits was achieved in the end of 1960's (Traub and Nomura 1968, Nomura and Erdmann 1970). This was soon taken advantage of and neutron scattering studies utilising selective

deuteration of the constituent proteins and variation of the scattering contrast of the aqueous buffer followed. The first attempts provided a set of distances between ribosome proteins (Hoppe 1973, Engelman et al. 1975) and the application of the method culminated in the low resolution structure of *E. coli* ribosome (Svergun et al. 1997, Svergun and Nierhaus 2000).

Article II of this dissertation presents an application of neutron scattering, subunit deuteration and contrast variation to the structural study of the $\phi 6$ bacteriophage procapsid. Electron cryomicroscopy models of the procapsid show a protein shell consisting of structural protein P1 and a satellite structure in the fivefold vertex of the icosahedral procapsid, which corresponds to the RNA translocase, hexamer of P4 (de Haas et al. 1999). Positions of the two remaining proteins P2 and P7 could not be determined from the EM model, so procapsids with deuterated P2 and P7 were prepared and small angle neutron scattering measurements with varying contrast levels made. The scattering, interpreted in terms of procapsid model, gave estimates on the positions of these proteins.

2.3 Chlorosome

First observations of large scale photosynthetic antenna complexes in bacteria were made by Germaine Cohen-Bazire and coworkers, who found 30–40 nm wide and 100–150 nm long vesicles in green bacteria belonging to genus *Chlorobium* (Cohen-Bazire et al. 1964). The electron micrographs obtained from fixated and stained bacteria showed these bodies, then called chlorobium vesicles, to be attached to the cytoplasmic membrane of the cell. Depending on staining and fixation, they were found to be either electron transparent or to contain a fine structure of 12–20 Å wide fibrils. When the vesicles were isolated, they were found to contain almost all of the chlorophyll contained in the cell and shown to be part of the photosynthetic machinery of green bacteria. Later these bodies were found also in other genera than *Chlorobium* (Holt et al. 1966, Pfennig and Cohen-Bazire 1967) and were shown not to contain a lipid bilayer membrane, making the term vesicle a misnomer. The word chlorosome was then introduced as a name for these structures (Staehelin et al. 1978).

Presently, chlorosomes are known to belong to the photosynthetic machinery in two groups of bacteria, namely green sulfur bacteria (family *Chlorobiaceae*) and filamentous anoxygenic phototrophs (families *Chloroflexaceae* and *Oscillochloridaceae*) (Olson 1998, Blankenship et al. 1995). Filamentous anoxygenic phototrophs are also known as green non-sulfur bacteria or green filamentous bacteria. These two families are phylogenetically distant and their photosynthetic reaction centers differ considerably. Nevertheless they share an antenna complex which is qualitatively similar (but not quantitatively, chlorosomes from *Chloroflexi* are somewhat smaller).

The interest in chlorosomes stems partly from the fact that they are found in bacteria which inhabit very demanding ecological niches. Some chlorosome containing species of green sulfur bacteria are found deep underwater (Manske et al. 2005), some even so deep that the best photon source available

is the thermal radiation from underwater volcanic activity (Beatty et al. 2005). There is good reason to believe that the antenna complexes developed by these organisms are among the most efficient photon catchers in nature. The energy, or exciton transfer properties in these structures are also remarkable, as sub-picosecond lifetimes for energy transfer have been observed (Prokhorenko et al. 2000).

Photosynthesis in green sulfur bacteria involves various different structures. The final step of energy transfer in the antenna complex is charge separation, which occurs in the reaction center, a protein complex bound to the lipid bilayer forming the inner part of the cell wall. The iron-sulfur type reaction center resembles the photosystem I found in green plants (Büttner et al. 1992) and transfers electrons to ferredoxins, as well as creates the potential difference between the cytosol and periplasmic space, which in turn drives the ATP synthesis. Bound to the reaction centers in the cytosolic side lie trimers of the Fenna-Matthews-Olson (FMO) pigment protein complexes. The FMO-protein was the first chlorophyll containing protein structure to be determined at high resolution (Fenna and Matthews 1975, Matthews et al. 1979).

Above the reaction center and the FMO complexes is the antenna complex itself. The chlorosome is surrounded by a galactolipid monolayer, a structure which is somewhat of a rarity in nature. The tails of the lipids are pointing inwards, creating a hydrophobic environment inside the chlorosome. The monolayer contains a total of 10 different chlorosomal proteins, named CsmA, to CsmF, CsmH, CsmI, CsmJ and CsmX (Vassilieva et al. 2002). The CsmA protein is directly bound to the FMO complex, forming a paracrystalline structure called the baseplate (Staehelin et al. 1980). Other proteins are distributed in the lipid monolayer on the chlorosome surface and, accoording to cross-linking studies, tend to form homomultimers (Li et al. 2006).

The reaction center, FMO-complex and the CsmA protein contain or are bound to bacteriochlorophyll *a*. The largest fractions in the chlorosome interior are, however, the chlorosome chlorophylls or bacteriochlorophylls *c*, *d* or *e* (Figure 2.1). The green coloured green sulfur bacteria species, such as *Chlorobium tepidum*, contain mostly BChl *c* and the brown colored species, like *Chlorobium phaeovibrioides* and *Chlorobium phaeobacteroides*, have mainly BChl *e* (article IV). It is estimated that a single chlorosome from *C. tepidum* contains over 200000 molecules of BChl *c* (Montaño et al. 2003). The fact that the mass ratio of BChl *c* to protein is 2:1 (Chung et al. 1994) and the localisation of the proteins to the surface of the chlorosome leads to the conclusion that the pigments are not bound to protein matrix, but form aggregates. This, along with their large size, makes chlorosomes unique among photosynthetic antennae.

Other components of the chlorosome interior are various carotenoids and chlorobactenes. These are present with molar ratios varying from 1:4 to 1:11 when compared to the amount of the main bacteriochlorophyll component (Arellano et al. 2000). The chlorosomes also contain small amounts of quinones (Frigaard et al. 1997). The remarkable thing about the chemical structure of chlorosomal bacteriochlorophylls and the carotenoid components is the presence of long hydrophobic carbon chains. Bacteriochlorophyll *c* in green sulfur bac-

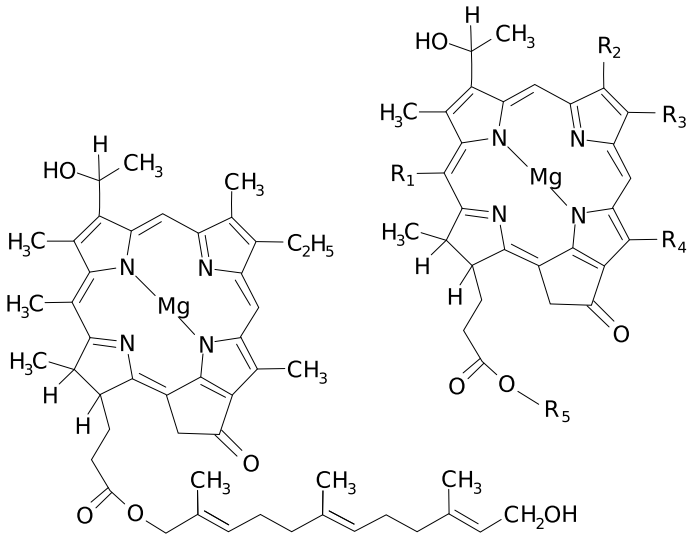

	Bacteriochlorophyll		
	c	*d*	*e*
R_1	Me	H	Me
R_2	Me	Me	CHO
R_3	Et, nPr, iBu	Et, nPr, iBu, neoPent	Et, nPr, iBu, neoPent
R_4	Me, Et	Me, Et	Et
R_5	Stearyl, Farn., others	Farn., others	Farn., others

Figure 2.1. Upper right: Chemical structure of bacteriochlorophylls, with the varying groups tabulated above. Lower left: Structure of bacteriochlorophyll *c* (farnesyl homologue). After (Blankenship et al. 1995).

teria is a mixture of both enantiomers and various homologues, which from the biosynthesis perspective seems to be an unnecessary complication. The length of the esterifying alcohol tail can vary widely. Farnesyl, phytyl and cetyl tails are usually present, with farnesyl being in majority, but a plethora of variations in esterifying alcohols exist in chlorosome chlorophylls (Francke and Amesz 1997).

The question of organisation of the pigment molecules inside the chlorosome, a major theme of this dissertation, has eluded definitive answers. Spectroscopic methods, mostly solid state NMR, have produced data on the local order and bonding patterns on BChls in native chlorosomes (Nozawa et al. 1994, Balaban et al. 1995, van Rossum et al. 2001). The results from these studies convincingly show that the $C3^1$-hydroxyl group of the BChl is coordinated to the magnesium of a neighbouring BChl. It may also be hydrogen bound to the $C13^1$-carbonyl group of a third BChl so that a kind of a two-dimensional lattice structure like the one shown in Figure 2.2 can in principle be formed.

The early work on the nanoscale structure found evidence of fibrils (Cohen-Bazire et al. 1964), but this model was soon abandoned. (Cruden and Stanier 1970) obtained EM images of chlorosomes with 10 to 25 circular structures 10 nm in diameter and with a 3 nm central hole in each chlorosome. Notably, the axis of symmetry of these circular structures was along the short axis of the chlorosome, in contrast to subsequent work.

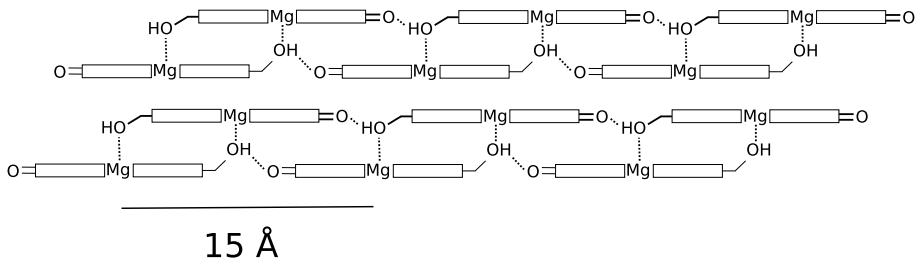

Figure 2.2. A possible bonding pattern of BChl molecules inside the chlorosome, after (Nozawa et al. 1994).

An influential pair of papers reporting freeze fracture electron microscopy results from filamentous anoxygenic phototroph *Chloroflexus aurantiacus* (Staehelin et al. 1978) and green sulfur bacterium *Chlorobium limicola* (Staehelin et al. 1980) appeared in the late 1970's. An internal structure consisting of 10 nm diameter rod elements was observed in freeze fracture images. In this work the rods were found to be oriented so that the symmetry axis was along the long axis of the chlorosome. This work laid the foundation to extensive modelling work, where structures satisfying the bonding patterns of Figure 2.2 were made to fill cylindrical structures (Nozawa et al. 1994, Holzwarth and Schaffner 1994, van Rossum et al. 2001). Exciton dynamics and energy transfer in these structures were also the subject of a very detailed analysis (Prokhorenko et al. 2000, Prokhorenko et al. 2003).

This dissertation presents results on the structure of the chlorosome interior which agrees with the first results of (Cohen-Bazire et al. 1964) (articles III, IV and V and section 4.3). This view is also supported by results of other groups (Hohmann-Marriott et al. 2005) and interestingly, also by some of the work from the original proponents of the rod element model (Figure 11 in (Sprague et al. 1981)).

3 Methods

3.1 Elastic scattering

In structural investigations of matter, elastic scattering of radiation such as photons, electrons and neutrons remains an important tool after nearly a century of use (Nobel prizes in Physics in 1914 to Max von Laue and in 1915 to W.H. Bragg and W.L. Bragg were awarded for the discovery and development of X-ray diffraction methods). The theory used to interpret the results of scattering experiments is simple and accurate, if care is taken not to violate its assumptions.

A beam of radiation, collimated so that the distributions in energy, direction and position in the plane transversal to propagation direction are sufficiently narrow, is brought to interact with a sample. The incident beam can be considered to consist of independent particles (or quanta) and at length-scales comparable to the sample features, they can be modelled by a plane wave. In elastic X-ray and neutron scattering, the differential cross section of the transition from incoming states with wave vector $\boldsymbol{k}$ to scattered states $\boldsymbol{k'}$ is given by the first order Born approximation in the product of the scattering field φ and a parameter ν describing the strength of its interaction with radiation (Merzbacher 1998, Feigin and Svergun 1987)

$$\frac{\mathrm{d}\sigma}{\mathrm{d}\Omega} = \left| \int e^{-i\boldsymbol{k'}\cdot\boldsymbol{r}} \nu\, \varphi(\boldsymbol{r}) e^{i\boldsymbol{k}\cdot\boldsymbol{r}} \mathrm{d}\boldsymbol{r} \right|^2 . \tag{3.1}$$

The quantity inside the absolute value bars in eq. (3.1) is called the scattering amplitude or scattering length. It can be written as

$$f(\boldsymbol{q}) = \int \nu\, \varphi(\boldsymbol{r}) e^{-i\boldsymbol{q}\cdot\boldsymbol{r}} \mathrm{d}\boldsymbol{r}, \tag{3.2}$$

where the difference of the scattered and incoming wave vectors $\boldsymbol{q} = \boldsymbol{k'} - \boldsymbol{k}$ is known as the scattering vector, wave vector transfer or momentum transfer (in units of $\hbar$).

The quantity probed in an elastic scattering experiment is thus the scattering length density $\nu\ \varphi(\boldsymbol{r})$, usually written as $\rho(\boldsymbol{r})$. The physical field $\varphi(\boldsymbol{r})$ corresponding to $\rho(\boldsymbol{r})$ varies with the type of radiation used. The major contributing fields to scattering length for commonly used types of radiation and the constants which couple the physical field values to scattering length density are given in Table 3.1.

Radiation	X-rays (1.5 Å)	Neutrons (1.8 Å)		Electrons (0.03 Å)
Interacting field φ	e^- density [m^{-3}]	Nuclear ρ [m^{-2}]		El. potential [V]
ν	$r_0\,(\mathbf{e}\cdot\mathbf{e}')$	1		$2\,\gamma\,m\,e/\hbar^2$
		H_2O	D_2O	
$\rho = \nu\varphi$ [10^{14} m^{-2}]	9.42	-0.56	6.40	102000
τ_{coh} [m]	0.1	10	0.08	$3 \cdot 10^{-10}$
τ_{tot} [m]	0.001	0.002	0.02	$1 \cdot 10^{-4}$

Table 3.1. Types of radiation, fields in matter causing most of the elastic scattering interaction with them, their coupling parameters ν (r_0 is the classical electron radius $e^2/(4\pi\varepsilon_0 m c^2)$, $\mathbf{e}$ and $\mathbf{e}'$ are the polarization vectors of incoming and scattered photons), their coherent forward scattering length densities ρ in water (also in heavy water for neutrons) and mean free paths in water corresponding to coherent interactions (τ_{coh}) and all interactions combined (τ_{tot}). The scattering length densities ρ are calculated from the atomic scattering amplitudes obtained from the International Tables for Crystallography, volume C. For electrons these are the Born electron scattering amplitudes. τ_{coh} is $(|f(0)|^2\,n)^{-1}$, where $f(0)$ is the molecular forward scattering amplitude. τ_{tot} is the inverse of linear attenuation coefficient for X-rays, inverse of the total macroscopic cross section for neutrons, and for electrons an estimate of the transport mean free path (Werner 2001).

In order for the simple scattering law of equation (3.1) to hold, the approximations made in deriving it need to hold for the experimental setup used. The far-field, or Fraunhofer approximation is validated by the fact that the transverse beam size is orders of magnitude smaller than the sample to detector distance in virtually every experimental apparatus.

The measurements presented in this dissertation are all made in the perpendicular transmission geometry. The Born first order, or single interaction approximation is valid in this kind of measurement setup when the sample thickness is such that the probability of one quantum of radiation having two elastic and coherent interactions with the sample is small enough. Table 3.1 gives the attenuation length of the coherent interaction[1] τ_{coh} for different types of radiation.

In the case of medium energy X-rays and thermal neutrons, the single interaction approximation is seen to be accurate for samples of macroscopic thickness. Indeed, the dynamics of matter-radiation interaction described by eq. (3.1) is so simple, that it is commonly called the kinematic scattering approximation. Nevertheless, for some measurement geometries, such as grazing incidence scattering from surfaces, this approximation is not valid. In these cases, further expansion of the Born series is necessary. An example relating to surface scattering is the distorted wave Born approximation (Rauscher et al. 1995), where the sample interaction is treated as a perturbation on the reflection of radiation from a flat surface, instead of perturbation on free propagation as in the standard Born approximation.

1. This number is a somewhat artificial measure of the strength of the interaction obtained by the formula $\tau_{el} = (|f(0)|^2\,n)^{-1}$, where $f(0)$ is the forward elastic scattering amplitude per molecule and n is the number density of molecules. Attenuation length τ is the depth where a particle has interacted with probability $1 - 1/e$.

Transmission electron microscopy or electron diffraction is in the domain of multiple scattering, as can be seen from table 3.1. Fortunately, thin low-Z samples such as biological matter can be treated in the weak phase object approximation, where only the phase of the incoming electron wave ψ_0 is perturbed by the projection of sample potential in the propagation direction, giving the transmitted wave as

$$\psi(\boldsymbol{r}) = \psi_0(\boldsymbol{r}) \exp(i\,\nu\,\lambda\,\varphi(x,y)) \approx \psi_0(\boldsymbol{r})(1 + i\,\nu\,\lambda\;\varphi(x,y)). \tag{3.3}$$

Here $\varphi(x,\,y) = \int\;\varphi(\boldsymbol{r}) - \bar{\varphi}\;\mathrm{d}z$ is the deviation of the projected potential from average value $\bar{\varphi}$ and $\nu = 2\,\gamma m\,e/\hbar^2$ (Cowley 1996, Wade 1992). This approximation rests on the fact that the atomic scattering factors for elastic electron scattering are strongly peaked in the forward direction, and that the cross sections of inelastic scattering and other processes which deflect electrons significantly from their trajectory are relatively small, as can be seen from the last column in the last row of table 3.1.

Electron microscopy of biological samples is thus phase contrast microscopy and depends on the manipulation of transmitted waves in the instrument. In modern transmission electron microscopes the phase difference between zero-order and diffracted waves is achieved by exploiting the hard-to-correct spherical aberration and combining it to various amounts of defocus. The end result is a phase transmission function resembling the Zernike phase plate used in optical phase contrast microscopy (Scherzer 1949). The Fourier transform of the intensity recorded in the image plane relates to the sample potential as

$$\tilde{I}\,(\alpha) = \delta(\alpha) + \nu\,\lambda\;\tilde{\varphi}\,(\alpha)\sin(2\,\pi\,W(\alpha)), \tag{3.4}$$

where α is the radial spatial frequency (or scattering angle) and $W(\alpha) \approx -\,\Delta f\,\lambda\,\alpha^2/2 + C_s\lambda\,\alpha^4$ is the wavefront aberration defined by the fixed spherical aberration coefficient C_s of the objective lens and the tunable defocus Δf (Erickson and Klug 1971). Inverse transform of (3.4) gives the relation between the image intensity and the potential φ as

$$I(x,y) = 1 + 2\,\nu\,\lambda\,\varphi(x,y) * s(x,y), \tag{3.5}$$

where star ($*$) denotes a convolution and $s(x,y)$ is the Fourier transform of the wave aberration, which can be seen to be the point spread function caused by the phase contrast imaging process.

3.2 Other processes

The theory of scattering described by equations (3.1) and (3.5) achieves its simplicity partly by ignoring beam-sample interactions which are not elastic and coherent. In a measurement, these processes contribute a signal which usually cannot be easily distinguished from elastic scattering. A good measurement setup will minimize the detectable effects of these processes, but their contribution still needs to be taken into account.

The quantity which determines the optimal sample thickness for X-rays is the cross section of total interaction, which largely consists of photoelectric effect, commonly referred to as absorption. For samples of biological origin, absorption is proportional to E^{-3}, while the elastic interaction decreases with increasing energy as E^{-2}. A wavelength of 1.5 Å (8.2 keV) with sample thickness of about 1 mm gives a good compromise between scattering length, absorption, sample thickness and easily obtainable radiation from X-ray tubes (the Cu K-L emission line has a wavelength of 1.54 Å).

The relaxation in the electronic structure of atoms following photoelectric excitation gives rise to fluorescence radiation. Depending on the atomic composition of the sample, this radiation can have wavelengths comparable to elastically scattered photons. The cross section of fluorescence is isotropic and causes a constant background in X-ray measurements. This constant is usually subtracted as a baseline, or taken into account by adding a constant term in intensity models. If a more quantitative approach is needed, the fluorescence intensity can be calculated based on the elemental composition of the sample and tabulated data (Brunetti et al. 2004).

Non-resonant X-ray scattering processes have a polarization dependency which is described by the differential Thomson cross-section. For an unpolarized X-ray beam it is (Warren 1969)

$$\left(\frac{\mathrm{d}\sigma}{\mathrm{d}\Omega}\right)_{\mathrm{Th}} = r_0^2 \frac{1}{2}(1+\cos^2(2\theta)), \tag{3.6}$$

where 2θ is the scattering angle. The inelastic, incoherent or Compton scattering of X-rays results in an additional background signal, which in angle dispersive measurements brings no information about the spatial distribution of electron density. The cross section of Compton scattering has an angular dependency which is almost opposite to the elastic scattering from isolated (i.e. gaseous) atoms. No incoherent intensity can be observed at scattering angle of zero, but as the scattering vector length increases, it starts to rise towards an asymptotic value (in units of Thomson cross-section) equal to the number of electrons in an atom. For modeling of elastic scattering, the contribution of inelastic scattering can be found from tabulated values of Compton scattering cross sections (Wang et al. 1993), when the atomic composition of the sample is known.

At high X-ray energies photons start to show additional interaction modes with matter. Above 1 MeV energy, pair production in nuclear and electron fields (Hubbell et al. 1980) and nuclear absorption are the dominant interactions, but in the 10 keV energy region typically used in structural studies, their effect is negligible.

The strength of coherent interaction of thermal neutrons with heavy water is of similar strength to X-rays, but other interactions are significantly weaker leading to a stronger scattering signal from thicker samples. The large difference in neutron scattering lengths between protonated and deuterated water gives the possibility of tuning the scattering length density of the water-based buffer solutions. This ability comes at the expense of the large incoherent scattering length density of protons, which gives a strong background.

For electrons, inelastic scattering cross section is not large when compared to elastic scattering. Together with forward peaked scattering amplitudes, this leads to long mean transport paths (Table 3.1). Nevertheless, in order to record coherent scattering events, very thin samples of the order of 100 nm are required in transmission geometry.

3.3 Classical theory of small-angle scattering

> It is very unlikely that any considerable progress will be made in the future.
>
> *André Guinier on theory of small-angle scattering (Guinier 1969)*

X-ray and neutron scattering probe the statistical ensemble, or bulk, of the microscopic structures contained in a sample. This is in contrast to microscopy techniques (such as TEM), which provide imaging information on selected microscopic portions of the sample and where the recorded image intensity corresponds to some intuitive measure of the density of the structure, such as the amount of electrons per area. Bulk methods provide average quantities, unless the structure under study is macroscopically simple, a single crystal for example.

The angle of attack for analysing scattering from natural, more or less disordered material is dependent on the amount of order in the sample under study. For polycrystalline solid materials, composed of small molecules, the powder diffraction method with Rietveld refinement (Rietveld 1969) will usually yield a solution with atomic resolution. Synthetic polymeric materials in solid state or melt can form amorphous or crystalline structures, but also various lamellar, micellar and cylindrical phases, which in principle diffract radiation like the atomic lattice in polycrystalline material. The structures are larger, which results in scattering to low scattering angles, according to the reciprocal relation between $\boldsymbol{q}$ and $\boldsymbol{r}$ in equation (3.2). Hence the technique is called small-angle scattering (SAS).

As for complex liquids, colloids or macromolecular complexes suspended in solution, no sharp diffraction peaks are usually observed. The methods for analysing small-angle scattering from this kind of solutions have developed significantly during the last 30 or so years, coinciding with increasing power of both computers and X-ray sources (but must be attributed mostly to development of computers). The theory of small-angle scattering was anyhow well developed before the age of computers.

The starting point of the analysis is the practical version of equation (3.1), the macroscopic cross section, or scattering intensity

$$I(q) = \frac{\mathrm{d}\Sigma}{\mathrm{d}\Omega} = \frac{1}{V_s}\left\langle \left| \int_{V_s} \rho(\boldsymbol{r}) e^{-i\boldsymbol{q}\cdot\boldsymbol{r}} \mathrm{d}\boldsymbol{r} \right|^2 \right\rangle_{\Omega}, \tag{3.7}$$

where $\langle\rangle_{\Omega}$ denotes orientational average over the ensemble of (assumedly) directionally isotropic microscopic structures. The function describing the structure in direct space, $\rho(\boldsymbol{r})$, is the excess scattering length density of the sample. It is the positive or negative deviation from the average scattering length density of the undisturbed bulk solvent, polymer or in the case of crystalline samples, vacuum. The irradiated volume of the sample is denoted by V_s.

For polycrystalline samples the treatment of equation (3.7) proceeds as is usual in the case of crystalline material, with the introduction of reciprocal lattice, Miller indices and the Laue conditions of diffraction, but with the additional difficulty caused by the loss of information due to orientational averaging. The theory of diffraction from polycrystalline materials is not the main interest in this dissertation (for comprehensive treatments, see (Klug and Alexander 1974) or (Warren 1969)). Here we only give the very basic results for reference. The Bragg equation

$$d = \frac{2\,\pi}{q} \tag{3.8}$$

gives the spacing d between crystal planes, or in the case of more complex materials, the distance between some other ordered scattering units, such as lamellae or tightly packed micelles, from the position q of a diffraction maximum. The Scherrer equation (Warren 1969)

$$L = \frac{5.6}{\Delta q} \tag{3.9}$$

can be used to estimate the lower limit to the linear size L of an ordered domain or microcrystal from the full width Δq of a Bragg diffraction maximum. For materials with low amount of order the domain size is not the only factor affecting the peak width, hence the Scherrer equation underestimates the domain size and only gives an order of magnitude estimate.

The quantity inside the angle brackets in equation (3.7) can be written as

$$\int \left[\int \rho(\boldsymbol{r}+\boldsymbol{u})\,\rho(\boldsymbol{u})\,\mathrm{d}\boldsymbol{u} \right] e^{-i\boldsymbol{q}\cdot\boldsymbol{r}} \mathrm{d}\boldsymbol{r} \tag{3.10}$$

and the function inside the brackets is the convolution of the excess scattering length density by the spatial inverse of itself, known in crystallography as the Patterson function (Klug and Alexander 1974) or characteristic function $\gamma(\boldsymbol{r})$. This function is symmetric, and is thus the Fourier pair of the real quantity $I(\boldsymbol{q})$, the unaveraged experimental intensity

$$I(\boldsymbol{q}) = \frac{1}{V_s} \int \gamma(\boldsymbol{r}) e^{-i\boldsymbol{q}\cdot\boldsymbol{r}} \mathrm{d}\boldsymbol{r}. \tag{3.11}$$

The Patterson function is the direct space representation of all the information obtained from a single crystal diffraction experiment (not including the various tricks, usually based on anomalous dispersion of atomic scattering factors, which can be used to get crystallographic phase information experimentally). Applying orientational averaging to equation (3.10) gives the isotropic version of the Patterson function, $p(r)$, defined as (Glatter and Kratky 1982)

$$I(q) = 4\,\pi \int_0^\infty p(r) \frac{\sin(q\,r)}{q\,r} \mathrm{d}r. \tag{3.12}$$

The $p(r)$ function is commonly employed in the analysis of colloidal substances in solution, which is also our focus, but a similar function is employed in the structural analysis of molecular liquids (Wagner 1972) and amorphous solids and glasses (Wagner 1978) as well.

If the sample consists of non-interacting and rigid particles in low concentration suspended in solution, the scattering signal can be approximated to originate from a single spherically averaged particle. As equation (3.12) is in principle invertible, the $p(r)$ function contains all the real space information that can be obtained from a solution scattering experiment.

To illustrate the type of information one obtains from $p(r)$, it is useful to imagine a particle with a homogeneous excess scattering length density and a clear boundary, an approximation which is often valid for proteins. The $p(r)$ is related to the averaged characteristic function $\gamma(r)$ of a particle by $p(r) = r^2 V\gamma(r)$, where V is the particle volume. In the case of a homogeneous particle, the $\gamma(r)$ gives the probability of finding a point which is inside the particle, at the end of randomly oriented vector of length r, when starting from a random point inside the particle.

From equations (3.7) and (3.10) it is easily seen that the intensity at zero angle $I(0)$ is proportional to the square of the total excess scattering length of the particle, $I(0) = \langle\rho\rangle^2 V^2$. If intensities can be measured in absolute units, that is, the mass concentration of the sample is known and incoming radiation dose falling into the sample during measurement can be measured accurately, then the molecular mass of the particle can be obtained from $I(0)$. In addition, one needs to know the average scattering length per volume and per molecular mass, which are easy to obtain for proteins. For X-rays, the explicit formula for molecular mass determination is given as (Koch et al. 2003)

$$M = \frac{I(0)}{c} \frac{\mu^2}{N_A(1-\rho_0\psi)^2}, \tag{3.13}$$

where c is the mass concentration, ρ_0 is the average scattering length density of the solvent, N_A is the Avogadro's number, and μ and ψ are the ratios of the particle molecular mass and volume to its scattering length. For X-ray scattering of proteins, in electron units, μ has a value of 1.87 g/(mol $\cdot\, r_0$), and ψ is 2.38 Å$^3/r_0$. The X-ray scattering length densities of water (ρ_0) and protein (inverse of ψ) are 0.334 r_0/Å^3 and 0.42 r_0/Å^3, respectively.

In routine practice, scattering intensities are often not measured in absolute units. If molecular mass is desired from a small-angle scattering experiment (for mass determination only, other methods are often preferable for their simplicity and smaller sample quantity requirements), it is easier to measure a well characterised standard sample, where the ratio after $I(0)/c$ in equation (3.13) is the same as in the sample under study, and keep measurement parameters strictly identical for the sample and standard. The ratio of molecular masses can then be obtained simply from the ratio of $I(0)$ of the sample and standard. In protein solution work, the standard sample is often bovine serum albumin (BSA) solution with a concentration of about 5 g/l.

A theoretician might be pleased with equation (3.13), but a practical scientist is not happy; the measurement of zero angle scattering is always going to be impossible, due the zero angle being occupied by the primary beam. As was made clear before, the majority of the incident radiation in a properly setup X-ray or neutron scattering experiment does not interact with the sample, at least not in a way which would be useful for our purposes, making the primary beam orders of magnitude more intense than the scattered radiation. This problem is overcome by the use of perhaps the most famous formula in the field of small-angle scattering, the Guinier relation, discovered by André Guinier and published in his Ph.D thesis (Guinier 1939)

$$I(q) = I(0)\exp(-R_g^2 q^2/3), \text{when } R_g^2 q^2 \ll 1. \tag{3.14}$$

The parameter R_g is known as radius of gyration. The Guinier relation can be derived from equation (3.12) by expanding the sinc-function term as a power series. The radius of gyration is then related to integrals over the $p(r)$ function and also to the distribution of excess scattering length density by (Vachette and Svergun 2000)

$$R_g^2 = \frac{\int p(r) r^2 \mathrm{d}r}{2\int p(r)\mathrm{d}r} = \frac{\int \rho(\boldsymbol{r})\boldsymbol{r}^2 \mathrm{d}\boldsymbol{r}}{\int \rho(\boldsymbol{r})\mathrm{d}\boldsymbol{r}}, \tag{3.15}$$

where in the integral over $\rho(\boldsymbol{r})\,\boldsymbol{r}^2$, the origin of vector $\boldsymbol{r}$ must be the center of mass of $\rho(\boldsymbol{r})$. Equation (3.14) allows the determination of two important parameters from a single plot of $\ln I(q)$ versus q^2, namely the zero-angle intensity, related to molecular mass, and a parameter related to the overall size of the particle, the radius of gyration. It is valid for any shape of particle, but for globular shapes its validity continues in practice to larger q-values than given in equation (3.14), usually up to $R_g q \approx 1.2$. Other formulas similar to the Guinier relation exist for rods, platelets and other basic shapes which are applicable in a larger angular range (Feigin and Svergun 1987).

Two well known equations in the classical treatment of small-angle scattering are credited to G. Porod. Inverting equation (3.12) leads to an equation for $p(r)$, or the characteristic function $\gamma(r)$, and intensity

$$p(r) = Vr^2\gamma(r) = \frac{1}{2\pi^2}\int_0^\infty q\, r\, I(q)\sin(q\, r)\mathrm{d}q. \tag{3.16}$$

Taking the limit $r \to 0$ results in

$$V\gamma(0) = \frac{1}{2\pi^2}\int_0^\infty q^2 I(q)\mathrm{d}q \equiv Q,$$

where Q is the Porod invariant (Porod 1951). The definition of the characteristic function $\gamma(\boldsymbol{r})$ in equation (3.10) shows that $\gamma(0)$ is equal to the average of the square of excess scattering length density, thus

$$Q = V\langle \rho^2 \rangle.$$

This expression does not depend on the structure of the system under study, only on its scattering contrast.

Porod also showed that for a particle with homogeneous scattering length density and well defined surface, the high-q limit of the Porod plot, $q^4 I(q)$ versus q is related to the surface area S of the particle as

$$8\pi^3 \lim_{q\to\infty} q^4 I(q) = S\langle \rho^2 \rangle + B\, q^4. \tag{3.17}$$

In other words, the specific surface S/V can in principle be determined from the invariant Q and a high-q fit to the Porod plot. Unfortunately the scattering signal from solutions is usually rather weak in the high angles, making the accurate determination of the specific surface difficult.

When one is interested in only the scattering from the shape of the particle (and thus trying to ignore the internal structure), one approximation involving the Porod law is to subtract from the intensity curve a constant B obtained from a fit to equation (3.17) (Koch et al. 2003). The rationale behind this is that contributions from inhomogeneities and incorrect background subtraction result in an approximately constant extra term in the intensity, which is removed by forcing $I \sim q^{-4}$ behaviour in large angles.

3.4 Direct modeling of small-angle scattering

Intensity of small-angle scattering contains more information than the integral parameters like molecular mass, radius of gyration or specific surface, which were presented in the previous section. On the other hand the information content in small-angle scattering is not enough for models to be formed deductively, so one has to resort to hypothesis testing. This is usually made by finding the least incompatible model from a class of models which are suitably parametrised. The figure of merit used in comparing the model and data is nearly always χ^2, the inverse variance weighed sum of squares of differences between experimental and model-derived datapoints. The method is thus commonly called least-squares fitting (Press et al. 1992).

The $p(r)$ function, being an invertible transform of the intensity, contains in principle all the information contained in a scattering experiment, so the comparison of data to model could be made by calculating a theoretical $p(r)$ function and comparing it to the experimental one. In practice the derivation of $p(r)$ from experimental data is an ill-posed problem due to finite q-range, statistical uncertainty in the measurement and above all, non-ideal experimental apparatus. While methods based on indirect Fourier transform, regularization and heuristic criteria can often calculate the $p(r)$ to reasonable accuracy (Glatter 1977, Svergun et al. 1988), the comparison of model to data is more reliable in reciprocal space.

The averaged scattering intensity of a single particle, often called the form factor can be approximated by simple geometrical shapes of homogeneous density. The functions obtained from plugging these shapes into equation (3.7) can be found in textbooks (Feigin and Svergun 1987, Glatter and Kratky 1982) and review articles (Pedersen 1997). As an example, the form factor of a sphere of radius R can be found from the square of its scattering amplitude as

$$P_s(q,R) = \left[\frac{3\left(\sin(qR) - qR\cos(qR)\right)}{(qR)^3} \right]^2. \tag{3.18}$$

Scattering from a combination of spherically symmetric scattering centers can be combined with the formula first obtained by Peter Debye (Debye 1915)

$$I(q) = \sum_{m,n} f_m(q) f_n(q) \frac{\sin(q r_{mn})}{q r_{mn}}, \tag{3.19}$$

where $f_m(q)$ is the scattering amplitude of the center m and r_{mn} is the distance between centers m and n.

In article III scattering from a proposed model of BChl c organization inside the chlorosome (van Rossum et al. 2001, Prokhorenko et al. 2000) was compared to experimental results. The model consists of hollow[2] cylinders of equal length arranged as a small aggregate where the cylinders stand on a plane and their axis of symmetry points to the same direction. The non-averaged form factor of a cylindrical shell with inner radius R_1, outer radius R_2 and height H is

$$P_c(R_1, R_2, H, q, \theta) = \left[2\,\mathrm{sinc}(q\cos\theta\, H/(2\pi)) \frac{R_2 J_1(q\sin\theta R_2) - R_1 J_1(q\sin\theta R_1)}{q\sin\theta(R_2^2 - R_1^2)} \right]^2, \tag{3.20}$$

where θ is the angle between the scattering vector and the cylinder axis and $\mathrm{sinc}(x) = \sin(2\pi\ x)/(2\pi\ x)$. The Debye equation with identical, non-spherical scattering centers in identical orientations is

$$I(q) = \left\langle P(\boldsymbol{q}) \sum_{jk} \exp(i\boldsymbol{q}\cdot|\boldsymbol{r}_j - \boldsymbol{r}_k|) \right\rangle_\Omega. \tag{3.21}$$

Performing the averaging for a cylindrically symmetric $P(\boldsymbol{q})$ gives

$$I(q) = \frac{1}{2}\int_0^{\pi/2} d\theta \sin\theta\, P_c(q,\theta) \sum_{jk} J_0(q\sin\theta\, r_{jk}), \tag{3.22}$$

which can be considered to be a Debye equation for randomly oriented aggregates consisting of identical, oriented and cylindrically symmetric objects located on a plane which is normal to their axis of symmetry. Scattering calculated from this formula plus a background term was found to be incompatible with experimental results from chlorosome (article III, Figure 3).

2. Hollow meaning here that the scattering length density inside the cylinders is equal to the density surrounding the cylinders.

The approximation of non-interacting particles in solution is often but not always valid. For dilute solutions of biomacromolecules, the usual deviation from this approximation comes in the form of non-specific attractive interactions which appear as an effective increase in molecular mass and R_g, visible in the scattering curve as sharp increase in intensity at the very low angles. Concentrated solutions of charged colloids, such as polyelectrolytes, may exhibit the opposite behaviour and show signs of repulsive interactions, manifested by a decrease of intensity at the small angles. Analytical structure factors for simple interactions such as hard sphere potential or screened coulomb potential exist (Pedersen 1997) and can be used in modelling this kind of systems.

Finite beam size, spread in the wavelength of incoming radiation and other effects related to the measurement setup also have to be taken into account, although modern point-focusing instruments (section 3.6.1) with two-dimensional detectors have reduced the need for extensive corrections. The effect of a particular measurement setup to ideal data, often called instrumental smearing is fortunately a linear transform, although the kernel of the transform in the general case is more complicated than a simple convolution (Glatter and Kratky 1982).

It is often the case that the structure of the scattering particle or a part of it has a known crystallographic structure and the object of the solution scattering experiment is to determine the structure of a conformational isoform or binding state in solution (article I). The Debye equation (3.19) can be used to calculate the solution scattering from an atomic model, when the $f(q)$'s are substituted with atomic scattering factors, but this only gives the scattering in vacuum, discarding the contribution of the solvent. Proteins have been shown to interact with aqueous solvent so that a hydration layer about 10% thicker on the average than the bulk solvent forms to the surface of the molecule (Svergun et al. 1998). This can be taken into account in the atomic model by adding a mesh of dummy solvent scatterers to the surface of the model (Svergun et al. 1995).

A method of calculating and modelling of small-angle scattering with considerable theoretical and computational appeal is the expansion of scattering amplitudes with a series of spherical harmonics (Stuhrmann 1970, Svergun 1991). This representation of the scattering amplitudes is especially useful for rigid body modelling of subunits (Petoukhov and Svergun 2005).

3.5 Contrast variation

Additional information from small-angle scattering can be obtained if the scattering length density of the solvent can be changed. In the case of single compact particle the function $\rho(\boldsymbol{r})$ describing the structure can be decomposed into parts corresponding to the shape, or the outline of the particle and internal fluctuation around the average excess scattering length density (Stuhrmann and Miller 1978)

$$\rho(\boldsymbol{r}) = \Delta\rho\,\rho_c(\boldsymbol{r}) + \rho_s(\boldsymbol{r}). \tag{3.23}$$

The average contrast between the particle and solvent is denoted by $\Delta\rho$, the shape function which is 1 inside the particle and 0 outside by $\rho_c(\boldsymbol{r})$, and the internal fluctuations of the scattering length density by $\rho_s(\boldsymbol{r})$. Performing the transforms of equation (3.7) gives the measured intensity as a sum of three basic scattering functions

$$I(q) = (\Delta\rho)^2 I_c(q) + \Delta\rho\, I_{\mathrm{cs}}(q) + I_s(q). \tag{3.24}$$

The contributions are from the shape $I_c(q)$ and the fluctuations $I_s(q)$ and their cross term $I_{\mathrm{cs}}(q)$. As the multipliers of the three functions are linearly independent, it is obvious that if scattering from three or more levels of contrast $\Delta\rho$ can be measured, the functions can be, in principle, solved. Single particle contrast variation has been used mainly determining the shape of the particle (Svergun and Stuhrmann 1991), but also in the analysis of internal fluctuations (Svergun 1994).

Labeling of subunits in a large complex will lead to equations similar to equation (3.24), now the contrast level in the unlabeled part is $\rho_a - \rho_0$ and in labeled part $\rho_b - \rho_0$, where ρ_0 is the solvent scattering length density. The intensity is then given as

$$I(q) = (\rho_a - \rho_0)^2 I_a(q) + (\rho_a - \rho_0)(\rho_b - \rho_0) I_{ab}(q) + (\rho_b - \rho_0)^2 I_b(q) \tag{3.25}$$

and again, the ability to change only one of the contrasts ρ_a, ρ_b or ρ_0 at will allows to solve for the scattering of the parts and the cross term.

This kind of technique was used in article II to determine the positions of two protein components in the procapsid of bacteriophage $\phi 6$ by small-angle neutron scattering and deuterium labeling of one protein at a time. Unfortunately the concentrations where the sample would remain monodisperse were so low, that full solution of equations (3.25) was not possible due to noisy scattering curves. Instead of contrast variation, a contrast matching experiment was made. The scattering length density of the buffer solution was set to match the unlabeled protein part of the procapsid by adjusting the ratio of D_2O to H_2O to 40%, resulting in a scattering curve where only the contribution of the labeled part was observable.

Deuterium labeling and changing the D_2O / H_2O ratio are not the only mechanisms available for varying contrast. With X-rays there exists the possibility of changing the density of the solvent by adding large concentrations of soluble molecules such as sucrose (Svergun et al. 1994), although this method is rarely used. If significant concentrations of heavy elements exist either in the solvent or the solute, the resonant "anomalous" scattering of these atoms in a selected absorption edge can be used to vary the contrast (Fuoss et al. 1981, Stuhrmann and Notbohm 1981). Finally, there exists the possibility of using polarised neutrons with dynamic polarisation of hydrogen nuclei in the sample as a label (Knop et al. 1991), but the complex experimental setup required by this method has made its application a rarity.

3.6 Instrumentation

> ...no major change can be foreseen, unless the power of x-ray sources is increased by a factor of 10 or 100, which is rather unlikely.
>
> *André Guinier on the practice of small-angle scattering (Guinier 1969)*

3.6.1 The pinhole small-angle scattering instrument

The requirement of reasonable sample penetration and optimal ratio of coherent scattering events to other processes determine the best wavelength of X-rays in studies of organic matter to be around 1.5 Å or 8 keV in photon energy (Stuhrmann and Miller 1978). This combined with large structures leads to small scattering angles, which in combination with weak signals place strict requirements to the collimation of the beam.

As with any collection of large number of elementary objects, the state of a beam of photons, neutrons or electrons can be described by its phase space distribution. In classical mechanics, this distribution is 6-variate, giving the density of particles in the vicinity of given position and momentum coordinates. One is usually only interested in beam properties in some plane perpendicular to the mean propagation direction, reducing the number of coordinates to five. When describing the state of a beam, i.e. a collection of particles with a roughly uniform propagation direction, the natural variables for describing the directional (or momentum) part of this distribution are spherical coordinates, with the z-axis pointing to the mean propagation direction. In practice, the state of the beam is given as a marginal distribution in two Cartesian position coordinates in the plane of interest, a marginal distribution in the two angular coordinates in momentum and a marginal distribution in the radial coordinate of momentum, usually in units of energy or wavelength. The 5-dimensional state of the beam is so factored into 2+2+1 marginal distributions. Additionally the distributions are usually approximated as gaussians, so in the end the beam is described by five parameters, the full widths of horizontal and vertical spot size, horizontal and vertical divergence, and the energy distribution.

If a single figure of merit is needed, the obvious choice is brilliance, the number of photons per second divided by the spot size, divergences and energy distribution. Values for state of the art X-ray instrumentation (ID02, ESRF) are roughly 10^{12} photons per second (at 12 keV), 0.6×0.2 mm^2 spot size (horizontal $\times$ vertical), 70×25 μrad^2 divergence and energy resolution of the order of 1 eV, which gives a brilliance of 10^{16} at the sample.

The instrument of choice today for all but the very lowest angles is the pinhole SAS camera (Huxley and Brown 1967), which consists of a point source of radiation and an optical system, which monochromatizes the beam and collimates or focuses it to the detector plane (see (Zemb et al. 2003) and (Pedersen 2004) for modern laboratory versions).

The smallest angle achieved by the pinhole setup is proportional to the ratio of the source size and collimation length. Figure 3.1 presents a ray diagram of a simple focusing two-pinhole instrument after the focusing optics. The first slit or pinhole has width W, the second slit has width G, and the camera length and sample to detector distances are L and S, respectively. The minimal beamstop size B is defined by the X-ray source size and the quality of the focusing optics. If the second slit width G is defined by W and L, assuming perfect focusing, then the collimation limited minimum angle θ_C can be easily seen to be $\mathrm{atan}(\frac{W}{2L}\frac{3-S/L}{1-S/L})$ and the beamstop limited angle $\theta_B = \mathrm{atan}(\frac{W}{2L}\frac{B/W+S/L}{S/L})$. These functions are monotonically increasing and decreasing as a function of S/L, respectively. Solving for $\theta_B = \theta_C$ gives $\hat{S} = L\frac{B}{B+2W}$ and a smallest obtainable angle of $\mathrm{atan}\frac{B+3W}{2L}$ as a function of camera length, source size and quality of focusing.

Real instruments usually have a third slit to block the secondary scattering from the beam defining second slit. For strongly scattering samples, the minimum scattering angle can be calculated from the positions of the first slit (entry slit) and the last slit (guard slit) in the geometry of Figure 3.1. Weakly scattering samples require extremely low background levels, so positions of the two last slits in a three pinhole instrument, the beam defining slit and the guard slit should be used instead in the minimum angle calculation (Glatter and Kratky 1982).

Approximate values for a laboratory instrument are entry slit – detector distance $L = 3000$ mm, $W = 3$ mm and $B = 5$ mm, giving a minimum q of about 0.01 1/Å, when extremely low background levels are not needed. For example, the bacteriophage $\phi 6$ procapsid studied in article II has a radius of gyration of 200 Å. The Guinier approximation for a globular particle of this size is valid below $q = 0.006$ 1/Å, which makes the direct determination of the radius of gyration and zero-angle scattering impossible on this kind of instrument. The experiment described in article II was made on the neutron beamline D22 of the Institut Laue-Langevin, which has a total camera length of over 35 m and the neutron wavelength with the highest flux around 6 Å, making measurements of these small-angle parameters easy.

3.6.2 X-ray instrumentation

The development of X-ray sources probably surprised André Guinier[3] who made his discoveries with X-rays generated in vacuum tube based sources. The discovery of synchrotron radiation originating from accelerators and storage rings has increased the power of X-ray sources at an exponential rate. Since the 1960's the brilliance of the currently most powerful X-ray source in the world has, on the average, doubled every year (Raoux 1993). The much celebrated Moore's law has been true in the semiconductor industry during the same period, but the transistor densities double only every 18 months.

3. André Guinier was born in 1911 and died 3rd of July 2000 (Lambert 2001)

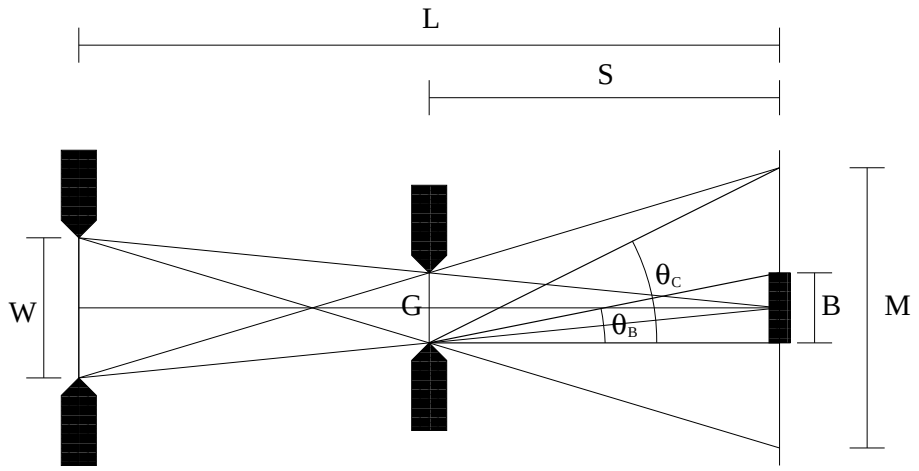

Figure 3.1. Ray diagram of a focusing two-pinhole camera of length L (the part after the optical system).

Nevertheless, in 1969 Guinier could have known better. The first synchrotron radiation absorption spectra were measured in 1965 by Japanese scientists, and in 1967 similar experiments were started at the DESY synchrotron in Hamburg (Robinson 2001). The development of synchrotron radiation sources can be described in terms of generations. First generation sources were shared machines where collision experiments for high energy physics and X-ray experiments were run intermittently. Second generation meant the first dedicated synchrotron light sources, and in third generation the storage rings were optimised for producing high-brightness beams with magnetic lattices designed to accommodate insertion devices. The first generation sources, such as the DORIS at DESY site in Hamburg are still in use, and the construction of fourth generation sources, the X-ray free electron lasers are underway.

After the X-ray source, a typical synchrotron small-angle X-ray scattering (SAXS) beamline has a channel cut crystal monochromator for narrow energy distribution and easy changing of wavelength for anomalous scattering experiments. The X-ray beam is focused by metal coated total external reflection mirrors to the detector plane. In laboratory instruments or fixed energy synchrotron beamlines the focusing in one of the directions is achieved by a curved monochromator. Multilayer mirrors have been recently introduced to both focus and partly monochromatize the beam in laboratory instruments, which leads to significant improvements in flux (Schuster and Gobel 1995). After the sample, the beam is transported in the characteristic element of SAXS beamlines, a large vacuum flight tube with a length ranging from one to ten meters and diameter defined by the detector size.

Detectors for small-angle X-ray scattering have developed from point detectors through linear gas detectors and quadrant detectors to two-dimensional position sensitive detectors. Area detectors are widely employed today in small-angle scattering as well as in other types of elastic X-ray scattering experiments. Different area detector types each have their advantages. Multiwire proportional chambers

are photon counting and thus have inherently excellent time resolution, as well as low background noise, but suffer from poor spatial resolution and inability to withstand high count rates (Né et al. 1997). Image plate detectors, being of integrating type do not suffer from high count rates and offer good spatial resolution, but have complex decay and background properties, which causes the dynamic range to be somewhat low, on the order of 10^4. The biggest problem with image plates is the long (minutes) read-out time, which makes this detector type impractical for time-resolved work (Né et al. 1993). This problem is somewhat less severe in CCD detectors fiber optically coupled to a scintillating material, which can be read in under a second. Mainly for this reason the CCD is the detector of choice for crystallography and general purpose elastic scattering beamlines at the moment. Near future should bring with it a detector type which combines the best features of both CCD coupled scintillators and gas-detectors. The pixel detector (Broennimann et al. 2006) has a "perfect" point spread function defined by the pixel size (currently 200×200 μm^2) and its readout time is under 10 ms, allowing time-resolved experiments.

3.6.3 Neutron instrumentation

From a user perspective, small-angle neutron scattering (SANS) beamlines differ from X-ray instruments largely by their low flux and large size, features which both arise from the low flux density in continuous reactor sources. The low flux means that a narrow wavelength distribution is not desirable. Resolution in small-angle scattering is not very sensitive to variation in wavelength, as is evident from the Ewald sphere. For this reason, the monochromators of choice in most SANS instruments are not crystals but mechanical chopping blades, or velocity selectors. These absorb neutrons travelling outside the desired speed, which in wavelength units is usually between 4 to 8 Å with a variation of 5 to 10%.

SANS beamlines on continuous neutron sources, such as the D22 in Institut Max von Laue – Paul Langevin in Grenoble are in some way the simplest form of a two-pinhole SAS instrument. The beam is not focused and the sample and detector are looking almost directly to the cold source (in practice the neutron guides are curved to remove the high energy neutrons). Collimation is adjusted by changing the length of a neutron guide with absorbing walls before the sample and by moving the detector inside the flight tube.

Detection of neutrons is made by a nuclear reaction in which the end products are energetic charged particles. The reaction $n+{}^3He \rightarrow {}^3H+{}^1H+0.764$ MeV is typically used and the scintillation caused by the fast charged end products in a suitable material is detected by image plates or banks of photomultipliers as in the 128×128 pixel multidetector at D22.

3.6.4 Electron cryomicroscopes

Electrons, being charged particles, can be focused with electromagnetic lenses so that the coherence of the scattered radiation is preserved to a high degree. This in principle allows imaging at atomic resolution.

The electron source in modern electron microscopes is a field emission tip, which has brightness many orders of magnitude larger than a typical synchrotron source (Spence and Howells 2002). The electron beam is accelerated to around 200-300 keV and focused by a condenser lens to impinge on the sample, which is mounted on a nanomanipulator stage. Objective and projector lenses then form an image, which is then recorded. Although CCD detectors for electrons exist, the detector of choice in imaging of biological samples is usually still photographic film, which offers the best spatial resolution and largest amount information per image (Zuo 2000).

Historically, the problem of biological EM has been the ambiguous results obtained by various different fixation and staining methods. Staining and fixation are required to make the sample withstand the ultra-high vacuum of the microscope column, give enough contrast for the structure under study to be detected in amplitude contrast, and make the sample resistant to the radiation dose from the imaging electrons. These problems are now somewhat alleviated by the invention of electron cryomicroscopy (Dubochet et al. 1988), in which the sample is fixated by embedding it in amorphous ("vitreous") ice formed by rapid cooling. The contrast is phase contrast, a much more suitable mechanism for low-Z materials and the radiation damage is reduced by the low temperatures. HRTEM images from crystalline inorganic substances already show individual atoms, so resolution in EM of biological matter is not limited anymore by the microscope, but by the ability of the sample to withstand radiation damage. Even cryo-EM reconstructions made from thousands of images of non-crystalline biological samples (mainly viruses and the ribosome) rarely reach resolutions significantly under 10 Å and single images, or tomography of non-identical particles are limited in resolution to 20 Å (Henderson 2004), which is roughly the size of the features studied in articles III, IV and V.

4 Results

4.1 Combining NMR and SAXS data

A method of constructing a structural model of a protein complex from known subunit models by SAXS and NMR residual dipolar couplings is presented in article I. The model substance used to demonstrate the method is calmodulin with its two globular domains connected by a flexible linker. Calmodulin in its Ca^{2+} form can be made to change conformation from elongated dumbbell shape to a compact globular form by adding a suitable binding molecule. In this case, the conformational change in calmodulin is affected by binding to 1 to 4 molecules of trifluoroperazine.

The polypeptide chain N-H residual dipolar couplings were measured from ^{15}N,^{1}H heteronuclear single quantum correlation spectrum in an aligned liquid crystal environment provided by filamentous phages. This provided the relative alignment of the two calmodulin domains in the tetrafluoroperazine bound structure.

Small-angle X-ray scattering provided data on the overall conformation of the complex. Both unbound and trifluoroperazine bound forms of calmodulin were measured. The $p(r)$ function and the radius of gyration obtained from solution scattering data showed significant differences between the two forms and indicated a more compact shape for the bound form. The SAXS data were further modelled by a rigid body refinement of the domains. The coordinates of the solution structure of unbound Ca^{2+} form of calmodulin (PDB code 1CLL) were split into parts corresponding to the two domains and their relative orientation was fixed to the value obtained from residual dipolar coupling measurements. The relative positions of the two domains were found by minimising the χ^2 between the scattering intensity calculated from the model by the Debye equation (3.19) and the experimental data as a function of the translation coordinates. Uncertainty in the coordinates obtained was determined by calculating the χ^2 of the fit around the minimum. The region of confidence was set to the volume in coordinate space where the χ^2 was less than 3.5 above the minimum.

The strongest signal in small-angle scattering is obtained near the zero angle and, as is well known, the first two terms in the expansion of small-angle scattering intensity about the origin correspond to the molecular weight and the radial distribution of scattering length about the center of mass, the R_g. It is therefore not surprising that the confidence region is well defined in the direction along the vector connecting the centers of masses of the domain (uncertainty ± 1 Å) and a larger uncertainty in position (± 4 Å) is found perpendicular to this direction (see Figure 3 of article I).

Combining SAXS and orientational information from dipolar couplings was found to be feasible in the case of a molecule where residual dipolar couplings can be successfully determined.

4.2 Subunit localisation in bacteriophage ϕ6

The nearly identical chemical properties of deuterium and hydrogen and the large difference in their neutron scattering length offer unique possibilities in labeling biological matter. Article II presents an application of deuterium labeling and solvent contrast variation to the study of structural biology of bacteriophage ϕ6.

Electron microscopy has traditionally been the tool of structural virology, but even with modern reconstruction methods, the resolution of three-dimensional electron density models does not allow the recognition of protein secondary structures. The overall architecture of the virus can be determined, and analysis of the binding properties of structural proteins allows their high resolution models to be fitted into the low-resolution structure. Non-structural proteins, such as the RNA polymerase P2 and packaging factor P7 of ϕ6 do not have clear binding sites and cannot be localised in the EM electron density map.

Neutron scattering measurements from two reconstituted samples of ϕ6 procapsids with P2 or P7 proteins deuterium labeled were made with varying amounts of solvent contrast, D_2O/H_2O ratios of 40%, 85% and 100% were used in the buffer solutions. Experiments were made difficult by aggregation of the procapsid in the sample solution, but a compromise between scattering intensity and monodispersity was found at 2 g/l procapsid concentration. Aggregation was still observed as an upwards deviation from the Guinier law behaviour in the very smallest angles, but larger angles showed a good fit to a monodisperse procapsid shell model with a 230 Å external and 100 Å internal radius.

The low concentration resulted in a weak scattering signal in the samples where the deuterium concentration was lower, as the incoherent scattering from solvent hydrogen nuclei increased the background considerably. The measurement made at 40% D_2O contrast contains in principle the information which was the goal of the experiment. This solvent contrast density matches the average scattering density of the unlabeled hydrated protein, leaving only the contribution of the deuterium labeled subunits visible in the low resolution structure. As solving the contrast variation equations implies increasing the noise further in the solution corresponding to the labeled subunits, modelling was based on the pure experimental 40% curve.

Stoichiometry of P2 (12 monomers per procapsid) and biochemical data lead to a model where the 40 Å diameter spherical proteins were placed in the five-fold axes of the icosahedrally symmetric virus. Optimisation of this model led to a distance of 110 Å, which matches the distance of the five-fold axis in the procapsid EM model, suggesting P2 association to this position.

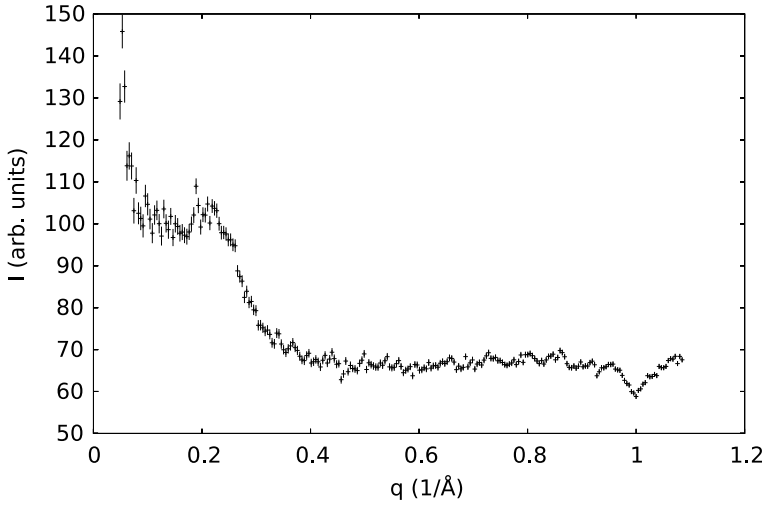

Figure 4.1. One of the first plots of X-ray scattering from chlorosomes. The sample is from *Chlorobium phaeobacteroides*.

The P7 is known to form elongated dimers and has a stoichiometry of 60 proteins per procapsid. This and a known function of accelerating the nucleation of P1-P4 complexes into a procapsid suggests a position near the two-fold symmetry axes (Poranen et al. 2001). A dimer model consisting of a 200 Å long string of 10 spheres with 20 Å diameter, was placed into the symmetry positions, and the distance from the center was obtained by a fit to the data. The distance was found to be 160 Å, localising the P7 inside the icosahedral procapsid structure.

4.3 Internal structure of chlorosomes

The chlorosome containing bacteria have been a subject of extensive study for over four decades. During this time the structural models of chlorosomes have been mostly based on electron microscopy and model building from spectroscopical data and on biochemical insights. The model of the BChl organisation inside the chlorosomes which seemed to explain the available experimental data was the rod element model first proposed in 1978 (Staehelin et al. 1978) and later expanded to include 10 nm rods observed in genus *Chlorobium* (Staehelin et al. 1980). To the best of the authors knowledge, the first X-ray scattering results from purified chlorosome solutions were published in article III. The first measurements on *Chlorobium phaeobacteroides* chlorosomes (Figure 4.1) already hinted that 10 nm cylinders could not explain the observed X-ray scattering. The only discernible feature in the first noisy scattering curves was a prominent peak corresponding to a 30 Å Bragg distance, but no signs of a cylindrical form factor were visible.

Further work on *Chlorobium tepidum* chlorosome solutions on a sealed tube X-ray source in Helsinki confirmed that also the 0.07 1/Å peak, which one would expect to be present on a hexagonal aggregate of 10 nm diameter objects was nowhere to be found (Figure 4.2), a result which was afterwards confirmed at the ultra-small-angle scattering beamline BW4 at Hasylab, Hamburg. In *C. tepidum*

chlorosomes, a prominent peak was found corresponding to a Bragg distance of 21 Å. Measurements at wider angles from concentrated solutions and dried powder samples also exhibited three more maxima at 12 Å, 9.4 Å and 8.2 Å (Figure 4.3).

Electron cryomicroscopy had at the same time revealed striations running parallel to the long axis of the *C. tepidum* chlorosomes. Fourier analysis of the EM images confirmed that the striations were well aligned with the chlorosome axis and had a spacing of around 20 Å. It was obvious that BChl molecules could not be arranged into cylinders with a diameter of 20 Å or so, as this would lead to a very dense packing and would not easily fulfil the requirement of Mg-coordination with $C3^1$-hydroxyl group of a neighbouring BChl, which is strongly suggested by various spectroscopies.

The simplest interpretation of the data was that the cylinder needed to be unrolled, so in article III, a lamellar structure was proposed for the BChl *c* and carotenoid organisation inside *C. tepidum* chlorosomes. In this model the BChl *c* molecules are organised in stacks, with the farnesyl tails pointing outwards perpendicular to the lamellae, and the carotenoid molecules being intermixed with the tails. Two models of the stack structure were proposed, both fulfilling the bonding patterns of BChl *c*: A stack consisting of enantiomerically pure BChl homologues, where the farnesyl tails all point to the same direction and a model where the tails extend to both sides of the stack, formed by dimers of BChl *c* containing molecules with both handedness. The latter model also has the virtue of forming a lattice which is compatible with the Bragg distances observed in the X-ray data, although from the widths of the diffraction maxima it is clear that this lattice has to be very disordered. Additionally, EM tilt series made from single chlorosomes suggested that the lamellae were undulating inside the chlorosome, which may explain the cylindrical structures observed in freeze-fracture electron microscopy.

Work on chlorosome characterisation was continued with structural studies on samples obtained from other *Chlorobium* species (article IV). The main bacteriochlorophyll homologue in *C. tepidum*, BChl *c*, is replaced by BChl *e* in brown colored green sulfur bacteria *C. phaeovibrioides* and *C. phaeobacteroides*. The carotenoid composition of *C. phaeovibrioides* chlorosomes was also manipulated by either growing the bacteria in the presence of 2-hydroxybiphenyl (HBP) which inhibits the carotenoid biosynthesis, or by extraction of carotenoids from purified chlorosomes by hexanol.

High performance liquid chromatography (HPLC) of the hexanol treated chlorosomes showed that the carotenoid content was significantly reduced when compared to the untreated control samples. Chlorosomes from bacteria grown with HBP also showed only small amounts of carotenoids, but phytoene, the immediate precursor in the carotenoid biosynthesis blocked by HBP, was shown to be accumulated to the chlorosomes in large numbers. Electron cryomicroscopy of *C. phaeovibrioides* chlorosomes revealed interesting differences when compared to *C. tepidum* chlorosomes. Striations of 21 Å to 25 Å were present, but were not continuous as in *C. tepidum*. Irregular domains were found, where the direction of the striations deviated randomly from the long axis of the chlorosome. The surface and the shape of the chlorosomes appeared rough, which seemed to be a result of the chlorosome being assembled from block-like BChl aggregates.

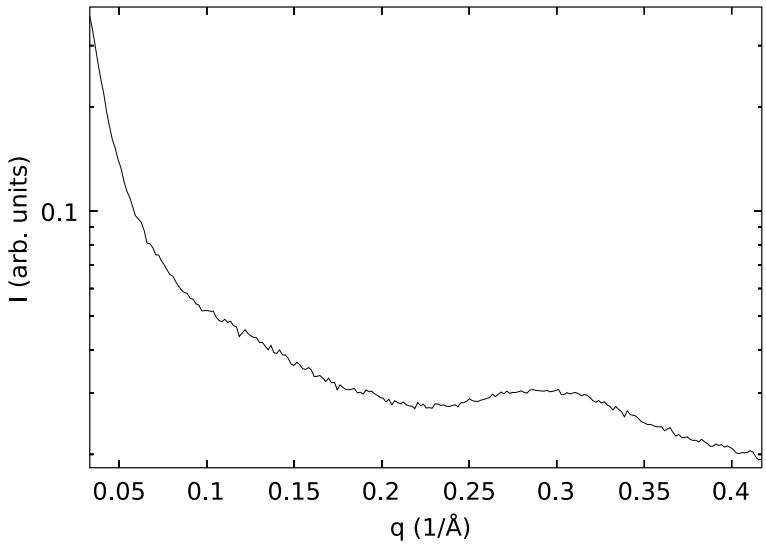

Figure 4.2. Low angle X-ray scattering from *Chlorobium tepidum* chlorosomes.

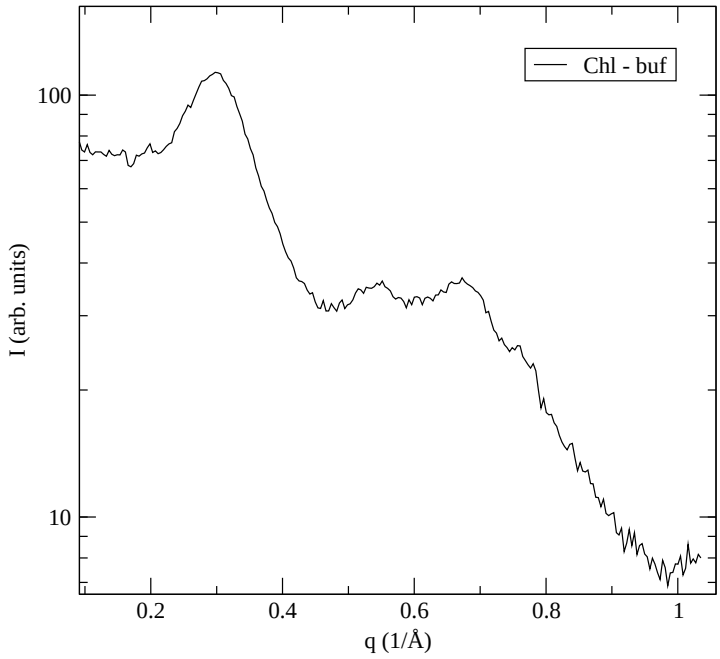

Figure 4.3. X-ray scattering from a concentrated solution of *Chlorobium tepidum* chlorosomes shows diffraction maxima at wider angles.

The X-ray scattering showed a prominent peak corresponding to Bragg distances between 27–30 Å in the wild type *C. phaeovibrioides* chlorosomes. The removal of carotenoids by hexanol caused a contraction in the spacing to 22 Å and widening of the diffraction maximum, proving that the carotenoids indeed form a part of the lamellar structure, but also that the fully assembled structure will

stay intact when the carotenoids are removed. The wide angle features observed in *C. tepidum* chlorosomes were completely absent in all the samples obtained from other species, indicating increased disorder.

Electron microscopy from *C. phaeobacteroides* chlorosomes revealed a feature which has potentially large implications for the interpretation of the apparent domain structure and their self-assembly. The micrographs contained images of two types of chlorosomes, one type with long striations oriented along the ellipsoid axis and having spacing of 27–33 Å, other type with a domain structure and smaller striation spacing of 21–26 Å. This first of all shows the considerable variability in the morphology of the chlorosomes, but also gives hints on how the domain structure is formed. The well ordered chlorosome may still be in an early stage of development, where the BChl aggregates are formed by nucleation on top of the membrane-bound baseplate structure. As the chlorosome is filled with more of the main BChl variant, maybe due to stress caused by low amount of light, the aggregates will form independently of the baseplate structure. For a low light organism this has the additional advantage of creating variation in the dipole moments of the BChls, increasing the probability that a photon with a random polarisation state will be captured.

The effect of carotenoid types and concentration to the chlorosome structure can be studied in a more delicate way by using the genetic transformability of *Chlorobium tepidum*. The biosynthesis of carotenoids and chlorobactenes in this bacterium is well characterised and can be manipulated by removing the genes coding the enzymes involved in it (Frigaard et al. 2004). Article V presents the results of structural characterisation of chlorosomes obtained from such knockout mutants.

The synthesis of carotenoids proceeds from the unconjugated geranylgeranyl pyrophosphate via several enzymes to long and conjugated pigment chains. Six of these enzymes were disabled and optical absorption, X-ray scattering and electron cryomicroscopy measurements were made from chlorosomes obtained from the knockouts. Optical absorption unsurprisingly showed an absorption band at 515 nm in chlorosomes which contained conjugated chains such as lycopene and later products in the pathway. The three samples where the synthesis were cut earlier did not show this band, but had a somewhat blueshifted absorpion peak at 735–745 nm, compared to the 750 nm obtained from the wild type, although this shift is well within the variation obtained from measurements of other wild type samples.

Electron micrographs from the three samples which did not contain conjugated carotenoids showed a mix of chlorosomes with native ellipsoidal morphology and irregular, round shaped chlorosomes which did not exhibit parallel striations. The 22 Å striations were present in the ellipsoidal chlorosomes, but were more disordered than in the wild type sample. The fraction of round chlorosomes decreased as the carotenoid composition became more native-like (i.e. the later in the biosynthesis pathway the knocked-out enzyme is). In the three samples with conjugated carotenoid chains the round chlorosomes without striations were not observed, although the size of the chlorosomes produced in these strains was smaller ((100–150) $\times$ 40 nm) than in the wild type.

The goal of the X-ray experiment described in article V was to test the hypothesis of carotenoid composition having an effect on structural parameters. The prediction of the lamellar model that carotenoids affect the lamellar distance was already shown to hold in article IV. Changing the carotenoid composition might have a more subtle effect, but as *C. tepidum* chlorosomes seemingly have an ordered structure giving more diffraction peaks, the effect would be easier to notice. An interesting question is the validity of the monoclinic lattice assigned to the wide angle scattering peaks in article III. According to this model, the reciprocal lattice vector corresponding to the lamellar diffraction maximum is perpendicular to the other assigned vectors, so that a change in lamellar spacing should have no effect on the positions of the other peaks.

The data, obtained mostly at the Hasylab small-angle scattering synchrotron beamline A2, contained evidence of the opposite. A change in lamellar spacing was observed in the samples containing non-conjugated carotenoid precursors. The distribution of the lamellar distance in these three samples was 23.5 ± 0.2 Å, while the wild type and the three samples containing conjugated chains had a lower mean lamellar distance of 22.2 Å with the standard deviation of 0.2 Å inside this group. This effect is expected in the light of carotenoid extraction and inhibition experiments from article IV, but a more surprising finding was similar behaviour in the large angle 8.2 Å peak for which a similar grouping produced a result of 8.280 ± 0.004 Å for the samples not containing conjugated chains and 8.220 ± 0.020 Å for the wild type and samples having the late stage biosynthesis products. The other two maxima in the wide angles did not show changes as a function of carotenoid composition within experimental precision. An obvious interpretation of this result would be that the wide angle peak is oriented in the same direction as the lamellar peak, contradicting the lattice assignment of article III.

The surprises from X-ray data did not end to unexpected peak shifts. A confirmation of a small sharp maximum at 0.2 1/Å, hints of which were seen in earlier measurements was obtained. This peak does not seem to correlate with the manipulation of carotenoid biosynthesis in any way, but stays constant from one sample to another. The small width of this maximum indicates that it could originate from a structure which is more ordered than the BChl stack, perhaps from the paracrystalline baseplate. The modulation in the baseplate lattice constant as a function of carotenoid composition could also explain the correlation between the lamellar distance and the 8.2 Å peak. If the baseplate acts as a nucleation template for the BChl aggregation, then modulations in its structure could also propagate to the lamellae. A new lattice assignment where these two small peaks are assigned to the baseplate is presented in article V.

Also, a broad feature was observed at 0.1 1/Å. Combinations of structure and form factors corresponding to domains in the BChl aggregates were calculated and fitted to experimental data, but no model in the size scale of the domains observed in EM was found to be satisfactory in explaining the data. Qualitatively the best fit was achieved by a simple form factor of a flat ellipsoidal cylinder 100 nm long, 50 nm wide and with a height distribution between 6 nm and 10 nm. Although the parametrisation used does not allow for quantitative fitting of the whole low-

angle data, the correspondance gives support for the idea that in the samples where this peak is prominent, there is a proportion of chlorosomes which are essentially not much more than a flat baseplate. Again, the samples in which this feature is the strongest are the ones where the carotenoid biosynthesis pathway is disrupted early. On the other hand, the possibility that this broad (FWHM ~ 0.1 $1/\text{Å}$) peak is a composite of two or more Bragg reflections from a disordered large scale structures cannot be ruled out completely.

All in all, new structural information on the chlorosome structure has caused renewed interest on the subject and re-evaluation of the old experiments. The results have also gained support from other research groups (Hohmann-Marriott et al. 2005, Balaban et al. 2005).

5 Concluding remarks

Since structural biology at atomic resolution was started by the pioneering works of Kendrew and Perutz (Kendrew et al. 1958, Kendrew et al. 1960, Perutz et al. 1960), improvements in the methodology of macromolecular crystallography have driven the size of known structures steadily upwards. The structure of ribosome, the molecular machine performing protein synthesis, was for a long time the objective of a concerted effort of many groups and various different methods, a sort of a holy grail of structural biology. After the first crystallographic structures of ribosomal subunits at what can be called an atomic resolution were published in 2000 (Ban et al. 2000, Wimberly et al. 2000), this work can be said to have reached at least a temporary conclusion. Although the amount of structural data in the protein data bank continues to grow at an exponential rate and automatisation of beamlines and crystallisation procedures allows this rate to continue, the grand challenges in methodology are found elsewhere.

As the rate limiting step in routine structure determination today is crystallisation, one of the challenges will be to develop methods which can resolve structures from non-crystalline samples. The methods used in this work, small-angle X-ray scattering, NMR, electron cryomicroscopy, neutron scattering with contrast variation and their combinations provide useful information from a sample in the solution state, but will not reach atomic resolution in their present incarnation. The future probably lies in single molecule methods, for which proposals using either X-rays or electrons as the imaging radiation exist. The X-ray method relies on femtosecond X-ray pulses obtained from the future free electron laser sources and the inertially limited nature of radiation damage (Neutze et al. 2000). Electrons, being somewhat more suitable for single molecule experiments due to their stronger interaction with matter (Henderson 1995), could be made to diffract from single molecules aligned by a powerful laser (Spence et al. 2005).

Still, even these proposed methods rely on the fact, curious by itself, that a large part of biological matter (mostly proteins and complexes of proteins and nucleotides) actually has a well defined structure which is identical in atomic resolution even in some large structures like the ribosome. As these methods replace the need for crystals by the need of thousands of single molecule images to form a three dimensional structure model, this requirement of coherence of spatial phases between individual particles is very strict. The chlorosome, it would seem, does not fulfill this requirement as its self-assembly is guided mostly by hydrophobic interactions instead of specific binding or folding of a polymer chain as in proteins. A student of photosynthetic antenna complexes in green bacteria will either have to wait for the breakthrough after the next breakthrough in methodology, or rely on experiments providing indirect information as has been the case so far.

Bibliography

Arellano J.B., Psencik J., Borrego C.M., Ma Y.Z., Guyoneaud R., Garcia-Gil J., Gillbro T. *Effect of carotenoid biosynthesis inhibition on the chlorosome organization in Chlorobium phaeobacteroides strain CL1401*. Photochemistry and Photobiology, 71: 715–723 (2000).

Babu Y.S., Bugg C.E., Cook W.J. *Structure of calmodulin refined at 2.2 A resolution.* Journal of Molecular Biology, 204(1): 191–204 (1988).

Balaban T.S., Holzwarth A.R., Schaffner K., Boender G.J., de Groot H.J. *CP-MAS 13C-NMR dipolar correlation spectroscopy of 13C-enriched chlorosomes and isolated bacteriochlorophyll c aggregates of Chlorobium tepidum: the self-organization of pigments is the main structural feature of chlorosomes.* Biochemistry, 34(46): 15259–15266 (1995).

Balaban T.S., Linke-Schaetzel M., Bhise A.D., Vanthuyne N., Roussel C., Anson C.E., Buth G., Eichhöfer A., Foster K., Garab G., Gliemann H., Goddard R., Javorfi T., Powell A.K., Rösner H., Schimmel T. *Structural characterization of artificial self-assembling porphyrins that mimic the natural chlorosomal bacteriochlorophylls c, d, and e.* Chemistry, 11(8): 2267–2275 (2005).

Ban N., Nissen P., Hansen J., Moore P.B., Steitz T.A. *The complete atomic structure of the large ribosomal subunit at 2.4 A resolution.* Science, 289(5481): 905–920 (2000).

Beatty J.T., Overmann J., Lince M.T., Manske A.K., Lang A.S., Blankenship R.E., Dover C.L.V., Martinson T.A., Plumley F.G. *An obligately photosynthetic bacterial anaerobe from a deep-sea hydrothermal vent.* Proc Natl Acad Sci U S A, 102(26): 9306–9310 (2005).

Blankenship R.E., Olson J.M., Miller M. *Antenna Complexes from Green Photosynthetic Bacteria*, chapter 20, pages 399–435. Kluwer Academic Publishers, Netherlands (1995).

Broennimann C., Eikenberry E.F., Henrich B., Horisberger R., Huelsen G., Pohl E., Schmitt B., Schulze-Briese C., Suzuki M., Tomizaki T., Toyokawa H., Wagner A. *The PILATUS 1M detector*. Journal of Synchrotron Radiation, 13(2): 120–130 (2006).

Brunetti A., del Rio M.S., Golosio B., Simionovici A., Somogyi A. *A library for X-ray matter interaction cross sections for X-ray fluorescence applications*. Spectrochimica Acta, B 59: 1725–1731 (2004).

Büttner M., Xie D.L., Nelson H., Pinther W., Hauska G., Nelson N. *Photosynthetic reaction center genes in green sulfur bacteria and in photosystem 1 are related.* Proc Natl Acad Sci U S A, 89(17): 8135–8139 (1992).

Chung S., Frank G., Zuber H., Bryant D.A. *Genes encoding two chlorosome components from the green sulfur bacteria Chlorobium vibrioforme strain 8327D and Chlorobium tepidum.* Photosynthesis Research, 41: 261–275 (1994).

Cohen-Bazire G., Pfennig N., Kunisawa R. *The fine structure of green bacteria.* Journal of Cell Biology, 22: 207–225 (1964).

Cowley J.M. *International tables for crystallography*, volume B, chapter 2.5.1, pages 281–290. Kluwer Academic Publishers, London (1996).

Cruden D.L., Stanier R.Y. *The characterization of chlorobium vesicles and membranes isolated from green bacteria.* Archives of Microbiology, 72(2): 115–134 (1970).

de Haas F., Paatero A.O., Mindich L., Bamford D.H., Fuller S.D. *A symmetry mismatch at the site of RNA packaging in the polymerase complex of dsRNA bacteriophage phi6.* Journal of Molecular Biology, 294(2): 357–372 (1999).

Debye P. *Zerstreeun von röntgenstrahlen.* Ann. Phys. (Leipzig), 46: 809–823 (1915).

Dubochet J., Adrian M., Chang J.J., Homo J.C., Lepault J., McDowall A., Schultz P. *Cryo-electron microscopy of vitrified specimens.* Quarterly Review of Biophysics, 21: 129–228 (1988).

Engelman D.M., Moore P.B., Schoenborn B.P. *Neutron scattering measurements of separation and shape of proteins in 30S ribosomal subunit of Escherichia coli: S2-S5, S5-S8, S3-S7.* Proc Natl Acad Sci U S A, 72(10): 3888–3892 (1975).

Erickson H.P., Klug A. *Measurement and compensation of defocusing and aberrations by fourier processing of electron micrographs.* Philosphical Transactions of the Royal Society of London B, 261: 105–118 (1971).

Feigin L.A., Svergun D.I. *Structure analysis by small-angle X-ray and neutron scattering.* Plenum Press, New York (1987).

Fenna R.E., Matthews B.W. *Chlorophyll arrangement in a bacteriochlorophyll protein from Chlorobium limicola.* Nature, 258: 573–577 (1975).

Fraenkel-Conrat H., Williams R.C. *Reconstitution of active tobacco mosaic virus from its inactive protein and nucleic acid components.* Proc Natl Acad Sci U S A, 41(10): 690–698 (1955).

Francke C., Amesz J. *Isolation and pigment composition of the antenna system of four species of green sulfur bacteria.* Photosynthesis Research, 52(2): 137 (1997).

Frigaard N.U., Maresca J.A., Yunker C.E., Jones A.D., Bryant D.A. *Genetic manipulation of carotenoid biosynthesis in the green sulfur bacterium Chlorobium tepidum.* Journal of Bacteriology, 186(16): 5210–5220 (2004).

Frigaard N.U., Takaichi S., Hirota M., Shimada K., Matsuura K. *Quinones in chlorosomes of green sulfur bacteria and their role in the redox-dependent fluorescence studied in chlorosome-like bacteriochlorophyll c aggregates.* Archives of Microbiology, 167: 343–349 (1997).

Fuoss P.H., Eisenberger P., Warburton W.K., Bienenstock A. *Application of differential anomalous X-ray scattering to structural studies of amorphous materials*. Physical Review Letters, 46: 1537–1540 (1981).

Glatter O. *A new method for the evaluation of small-angle scattering data*. Journal of Applied Crystallography, 10: 415–421 (1977).

Glatter O., Kratky O. *Small angle X-ray scattering*. Academic Press Inc., New York (1982).

Guinier A. *La diffraction des rayons X aux trés petits angles: application à l'étude de phénomènes ultramicroscopiques*. Annales de Physique (Paris), 12: 161–237 (1939).

Guinier A. *30 years of small-angle X-ray scattering*. Physics Today, 22(11): 25–30 (1969).

Henderson R. *The potential and limitations of neutrons, electrons and X-rays for atomic resolution microscopy of unstained biological molecules.* Quarterly Reviews of Biophysics, 28(2): 171–193 (1995).

Henderson R. *Realizing the potential of electron cryo-microscopy*. Quarterly Reviews of Biophysics, 37: 3–13 (2004).

Hohmann-Marriott M.F., Blankenship R., Roberson R.W. *The ultrastructure of Chlorobium tepidum chlorosomes revealed by electron microscopy*. Photosynthesis Research, 86: 145–154 (2005).

Holt S.C., Conti S.F., Fuller R.C. *Photosynthetic apparatus in the green bacterium Chloropseudomonas ethylicum.* Journal of Bacteriology, 91(1): 311–323 (1966).

Holzwarth A.R., Schaffner K. *On the structure of bacteriochlorophyll molecular aggregates in the chlorosomes of green bacteria. a molecular modelling study*. Photosynthesis Research, 41: 225–233 (1994).

Hoppe W. *The label triangulation method and the mixed isomorphous replacement principle.* Journal of Molecular Biology, 78(3): 581–585 (1973).

Hubbell J.H., Gimm H.A., Overbo I. *Pair, triplet, and total atomic cross sections (and mass attenuation coefficients) for 1 MeV-100 GeV photons in elements Z=1 to 100*. Journal of Physical and Chemical Reference Data, 9(4): 1023–1148 (1980).

Huxley H.E., Brown W. *The low-angle X-ray diagram of vertebrate striated muscle and its behaviour during contraction and rigor*. Journal of Molecular Biology, 30(2): 383–434 (1967).

Juuti J.T., Bamford D.H. *Protein P7 of phage phi6 RNA polymerase complex, acquiring of RNA packaging activity by in vitro assembly of the purified protein onto deficient particles.* Journal of Molecular Biology, 266(5): 891–900 (1997).

Kendrew J.C., Bodo G., Dintzis H.M., Parrish R.G., Wyckoff H.W., Phihips D.C. *A three-dimensional model of the myoglobin molecule obtained by X-ray anaysis*. Nature, 181: 666 (1958).

Kendrew J.C., Dickerson R.E., Strandberg B.E., Hart R.G., Davies D.R., Phillips D.C., Shore V.C. *Structure of myoglobin: a three-dimensional Fourier synthesis at 2 A resolution*. Nature, 185: 422 (1960).

Klug H.P., Alexander L.E. *X-ray diffraction procedures for polycrystalline and amorphous materials*. John Wiley & Sons, Inc., New York, second edition (1974).

Knop W., Hirai M., Olah G., Meerwinck W., Schink H.J., Stuhrmann H.B., Wagner R., Wenkowessouni M., Zhao J., Scharpf O., Crichton R.R., Krumpolc M., Nierhaus K.H., Niinikoski T.O., Rijllart A. *Polarized neutron-scattering from dynamic polarized targets in biology*. Physica B, 174(1-4): 275–290 (1991).

Koch M.H.J., Vachette P., Svergun D.I. *Small angle scattering: a view on the properties, structures and structural changes of biological macromolecules in solution*. Quarterly Reviews of Biophysics, 36(2): 147–227 (2003).

Lambert M. *André Guinier (1911-2000)*. Acta Crystallographica, A57: 1–3 (2001).

Li H., Frigaard N.U., Bryant D.A. *Molecular contacts for chlorosome envelope proteins revealed by cross-linking studies with chlorosomes from Chlorobium tepidum*. Biochemistry, 45(30): 9095–9103 (2006).

Makeyev E.V., Bamford D.H. *Replicase activity of purified recombinant protein P2 of double-stranded RNA bacteriophage phi6.* EMBO Journal, 19(1): 124–133 (2000).

Mancini E.J., Kainov D.E., Grimes J.M., Tuma R., Bamford D.H., Stuart D.I. *Atomic snapshots of an RNA packaging motor reveal conformational changes linking ATP hydrolysis to RNA translocation.* Cell, 118(6): 743–755 (2004).

Manske A.K., Glaeser J., Kuypers M.M.M., Overmann J. *Physiology and phylogeny of green sulfur bacteria forming a monospecific phototrophic assemblage at a depth of 100 meters in the Black Sea.* Applied and Environmental Microbiology, 71(12): 8049–8060 (2005).

Matthews B.W., Fenna R.E., Bolognesi M.C., Schmid M.F., Olson J.M. *Structure of a bacteriochlorophyll a-protein from the green photosynthetic bacterium Prosthecochloris aestuarii.* Journal of Molecular Biology, 131(2): 259–285 (1979).

Merril C.R., Scholl D., Adhya S.L. *The prospect for bacteriophage therapy in western medicine.* Nature Reviews Drug Discovery, 2(6): 489–497 (2003).

Merzbacher E. *Quantum mechanics*. John Wiley & Sons, Inc., New York, third edition (1998).

Mindich L. *Bacteriophage phi6: a unique virus having a lipid-containing membrane and a genome composed of three dsRNA segments*. Advances in Virus Research, 35: 137–176 (1988).

Mindich L., Bamford D. *Lipid-containing bacteriophages.*, volume 2, pages 475–520. Plenum, New York. (1988).

Montaño G.A., Bowen B.P., LaBelle J.T., Woodbury N.W., Pizziconi V.B., Blankenship R.E. *Characterization of Chlorobium tepidum chlorosomes: A calculation of bacteriochlorophyll c per chlorosome and oligomer modeling*. Biophysical Journal, 85: 2560–2565 (2003).

Né F., Gabriel A., Kocsis M., Zemb T. *Smearing effects introduced by the response function of position-sensitive gas detectors in SAXS experiments*. Journal of Applied Crystallography, 30(3): 306–311 (1997).

Né F., Gazeau D., Lambard J., Lesieur P., Zemb T., Gabriel A. *Characterization of an image-plate detector used for quantitative small-angle-scattering studies*. Journal of Applied Crystallography, 26(6): 763–773 (1993).

Neutze R., Wouts R., van der Spoel D., Weckert E., Hajdu J. *Potential for biomolecular imaging with femtosecond X-ray pulses.* Nature, 406(6797): 752–757 (2000).

Nomura M., Erdmann V.A. *Reconstitution of 50S ribosomal subunits from dissociated molecular components*. Nature, 228: 744–748 (1970).

Nozawa T., Ohtomo K., Suzuki M., Nakagawa H., Shikama Y., Konami H., Wang Z.Y. *Structures of chlorosomes and agregated BChl c in Chlorobium tepidum from solid state high resolution CP/MAS ^{13}C NMR.* Photosynthesis Research, 41: 211–223 (1994).

Olkkonen V.M., Bamford D.H. *The nucleocapsid of the lipid-containing double-stranded RNA bacteriophage phi6 contains a protein skeleton consisting of a single polypeptide species.* Journal of Virology, 61(8): 2362–2367 (1987).

Olkkonen V.M., Gottlieb P., Strassman J., Qiao X.Y., Bamford D.H., Mindich L. *In vitro assembly of infectious nucleocapsids of bacteriophage phi6: formation of a recombinant double-stranded RNA virus.* Proc Natl Acad Sci U S A, 87(23): 9173–9177 (1990).

Olson J.M. *Chlorophyll organization and function in green photosynthetic bacteria*. Photochemistry and Photobiology, 67(1): 61–75 (1998).

Pedersen J.S. *Analysis of small-angle scattering data from colloids and polymer solutions: Modeling and least-squares fitting*. Advances in Colloid and Interface Science, 70: 171–210 (1997).

Pedersen J.S. *A flux- and background-optimized version of the NanoSTAR small-angle X-ray scattering camera for solution scattering*. Journal of Applied Crystallography, 37: 369–380 (2004).

Perutz M., Rossmann M., Cullis A., Muirhead H., Will G., North. A. *Structure of haemoglobin. a three-dimensional Fourier synthesis at 5.5 A resolution, obtained by X-ray analysis*. Nature, 185: 416–422 (1960).

Petoukhov M.V., Svergun D.I. *Global rigid body modeling of macromolecular complexes against small-angle scattering data.* Biophysical Journal, 89(2): 1237–1250 (2005).

Pfennig N., Cohen-Bazire G. *Some properties of the green bacterium Pelodictyon clathratiforme*. Archives of Microbiology, 59(1): 226–236 (1967).

Poranen M.M., Paatero A.O., Tuma R., Bamford D.H. *Self-assembly of a viral molecular machine from purified protein and RNA constitutients*. Molecular Cell, 7: 845–854 (2001).

Porod G. *Die Röntgenkleinwinkelstreuung von dichtgepackten kolloiden Systemen, I*. Kolloidnyi Zhurnal, 124: 83–114 (1951).

Press W.H., Teukolsky S.A., Vetterling W.T., Flannery B.P. *Numerical Recipes in C, The Art of Scientific Computing*. Cambridge University Press, Cambridge, second edition (1992).

Prokhorenko V.I., Steensgaard D.B., Holzwarth A.R. *Exciton theory for supramolecular chlorosomal aggregates: 1. Aggregate size dependence of the linear spectra.* Biophysical Journal, 85(5): 3173–3186 (2003).

Prokhorenko V.I., Steensgard D.B., Holzwarth A.R. *Exciton dynamics in the chlorosomal antennae of the green bacteria Chloroflexus aurantiacus and Chlorobium tepidum*. Biophysical Journal, 79: 2105–2120 (2000).

Raoux D. *Neutron and synchrotron radiation for condensed matter studies*, volume 1 of *Hercules*, chapter 2, pages 37–78. Springer (1993).

Rauscher M., Salditt T., Spohn H. *Small-angle X-ray scattering under grazing incidence: The cross section in the distorted wave born approximation*. Physical Review B, 52(23): 16855–16863 (1995).

Rietveld H.M. *A profile refinement method for nuclear and magnetic structures*. Journal of Applied Crystallography, 2: 65–71 (1969).

Robinson A.L. *X-ray data booklet*, chapter 2.2, pages 2–17 – 2–23. Lawrence Berkely National Laboratory, University of California, Berkeley (2001).

Scherzer O. *The theoretical resolution limit of electron microscope*. Journal of Applied Physics, 20: 20–29 (1949).

Schuster M., Gobel H. *Parallel-beam coupling into channel-cut monochromators using curved graded multilayers*. Journal of Physics D: Applied Physics, 28(4A): A270–A275 (1995).

Shapiro D., Thibault P., Beetz T., Elser V., Howells M., Jacobsen C., Kirz J., Lima E., Miao H., Neiman A.M., Sayre D. *Biological imaging by soft X-ray diffraction microscopy.* Proc Natl Acad Sci U S A, 102(43): 15343–15346 (2005).

Spence J.C.H., Howells M.R. *Synchrotron soft X-ray and field-emission electron sources: a comparison.* Ultramicroscopy, 93(3-4): 213–222 (2002).

Spence J.C.H., Schmidt K., Wu J.S., Hembree G., Weierstall U., Doak B., Fromme P. *Diffraction and imaging from a beam of laser-aligned proteins: resolution limits*. Acta Crystallographica, A61(2): 237–245 (2005).

Sprague S.G., Staehelin L.A., DiBartolomeis M.J., Fuller R.C. *Isolation and development of chlorosomes in the green bacterium Chloroflexus aurantiacus.* Journal of Bacteriology, 147(3): 1021–1031 (1981).

Staehelin L.A., Golecki J.R., Drews G. *Supramolecular organization of chlorosomes (chlorobium vesicles) and of their membrane attachment sites in Chlorobium limicola*. Biochimica et Biophysica Acta, 589: 30–45 (1980).

Staehelin L.A., Golecki J.R., Fuller R.C., Drews G. *Visualization of the supramolecular architecture of chlorosomes (Chlorobium type vesicles) in freeze-fractured cells of Chloroflexus aurantiacus*. Archives of Mircobiology, 119: 269–277 (1978).

Stuhrmann H.B. *Interpretation of small-angle scattering functions of dilute solutions and gases. A representation of the structures related to a one-particle scattering function*. Acta Crystallographica, A26: 297–306 (1970).

Stuhrmann H.B., Miller A. *Small-angle scattering of biological structures*. Journal of Applied Crystallography, 11: 325–345 (1978).

Stuhrmann H.B., Notbohm H. *Configuration of the four iron atoms in dissolved human hemoglobin as studied by anomalous dispersion.* Proc Natl Acad Sci U S A, 78(10): 6216–6220 (1981).

Svergun D., Barberato C., Koch M.H.J. *CRYSOL – a program to evaluate X-ray solution scattering of biological macromolecules from atomic coordinates*. Journal of Applied Crystallography, 28(6): 768–773 (1995).

Svergun D.I. *Mathematical methods in small-angle scattering data analysis*. Journal of Applied Crystallography, 24: 485–492 (1991).

Svergun D.I. *Solution scattering from biopolymers: Advanced contrast-variation data analysis*. Acta Crystallographica, A50: 391–402 (1994).

Svergun D.I., Burkhardt N., Pedersen J.S., Koch M.H., Volkov V.V., Kozin M.B., Meerwink W., Stuhrmann H.B., Diedrich G., Nierhaus K.H. *Solution scattering structural analysis of the 70 S Escherichia coli ribosome by contrast variation. I. Invariants and validation of electron microscopy models.* Journal of Molecular Biology, 271(4): 588–601 (1997).

Svergun D.I., Nierhaus K.H. *A map of protein-rRNA distribution in the 70 S Escherichia coli ribosome.* Journal of Biological Chemistry, 275(19): 14432–14439 (2000).

Svergun D.I., Pedersen J.S., Serdyuk I.N., Koch M.H. *Solution scattering from 50S ribosomal subunit resolves inconsistency between electron microscopic models.* Proc Natl Acad Sci U S A, 91(25): 11826–11830 (1994).

Svergun D.I., Richard S., Koch M.H., Sayers Z., Kuprin S., Zaccai G. *Protein hydration in solution: experimental observation by X-ray and neutron scattering.* Proc Natl Acad Sci U S A, 95(5): 2267–2272 (1998).

Svergun D.I., Semenyuk A.V., Feigin L.A. *Small-angle-scattering-data treatment by the regularization method*. Acta Crystallographica, A44: 244–251 (1988).

Svergun D.I., Stuhrmann H.B. *New Developments in Direct Shape Determination from Small-angle Scattering. 1. Theory and Model Calculations*. Acta Crystallographica, A47: 736–744 (1991).

Traub P., Nomura M. *Structure and function of E. coli ribosomes, V. reconstitution of functionally active 30S ribosomal particles from RNA and proteins*. Proc Natl Acad Sci U S A, 59: 777–784 (1968).

Vachette P., Svergun D.I. *Structure and Dynamics of Biomolecules*, volume IV of *Hercules*, chapter 11, pages 199–237. Oxford University Press (2000).

van Rossum B.J., Steensgard D.B., Mulder F.M., Boender G.J., Schaffner K., Holzwarth A.R., de Groot H.J.M. *A refined model of the chlorosomal antennae of the green bacterium Chlorobium Tepidum from proton chemical shift constraints obtained with high-field 2-D and 3-D MAS NMR dipolar correlation spectroscopy.* Biochemistry, 40: 1587–1595 (2001).

Vandonselaar M., Hickie R.A., Quail J.W., Delbaere L.T. *Trifluoperazine-induced conformational change in Ca(2+)-calmodulin.* Nature Structural Biology, 1(11): 795–801 (1994).

Vassilieva E.V., Stirewalt V.L., Jakobs C.U., Frigaard N.U., Inoue-Sakamoto K., Baker M.A., Sotak A., Bryant D.A. *Subcellular localization of chlorosome proteins in Chlorobium tepidum and characterization of three new chlorosome proteins: CsmF, CsmH, and CsmX.* Biochemistry, 41(13): 4358–4370 (2002).

Vidaver A.K., Koski R.K., Etten J.L.V. *Bacteriophage phi6: a lipid-containing virus of Pseudomonas phaseolicola.* Journal of Virology, 11(5): 799–805 (1973).

Wade R.H. *A brief look at imaging and contrast transfer.* Ultramicroscopy, 46: 145–156 (1992).

Wagner C.N.J. *Diffraction analysis of liquid metals and alloys*, chapter 6, pages 257–329. Marcel Dekker, New York (1972).

Wagner C.N.J. *Direct methods for the determination of atomic-scale structure of amorphous solids (X-ray, electron and neutron scattering).* Journal of Non-Crystalline Solids, 31: 1–40 (1978).

Wang J., Sagar R., Schmider H., Smith V. *X-ray elastic and inelastic scattering factors for neutral atoms Z = 2-92.* Atomic Data and Nuclear Data Tables, 53: 233–269 (1993).

Warren B.E. *X-ray Diffraction.* Dover (1969).

Werner W.S.M. *Electron transport in solids for quantitative surface analysis.* Surface and Interface Analysis, 31: 141–176 (2001).

Wimberly B.T., Brodersen D.E., Clemons W.M., Morgan-Warren R.J., Carter A.P., Vonrhein C., Hartsch T., Ramakrishnan V. *Structure of the 30S ribosomal subunit.* Nature, 407(6802): 327–339 (2000).

Zemb T., Taché O., Né F., Spalla O. *A high-sensitivity pinhole camera for soft condenced matter.* Journal of Applied Crystallography, 36: 800–805 (2003).

Zuo J.M. *Electron detection characteristics of a slow-scan CCD camera, imaging plates and film, and electron image restoration.* Microscopy Research and Technique, 49: 245–268 (2000).